1-1-1968

Dynamic stress concentration using the photolaserelastic technique.

William G. James
University of Windsor

DYNAMIC STRESS CONCENTRATION USING THE PHOTOLASERELASTIC TECHNIQUE

A Thesis
Submitted to the Faculty of Graduate Studies through the
Department of Mechanical Engineering in Partial Fulfilment
of the Requirements for the Degree of
Master of Applied Science at the
University of Windsor

by

William G. James

Windsor, Ontario
1968

ABD5364

APPROVED BY: J. B. Hayward

Orville Lamm

W. North

103571

ABSTRACT

In this investigation the photoelastic technique was employed to determine the maximum dynamic stress concentration factors in a dynamically loaded strut due to symmetrically located elliptical discontinuity. The two parameters time after impact and size of discontinuity were considered. The struts were made from a high modulus photoelastic material and all ellipses were oriented with the major axis perpendicular to the longitudinal axis of the strut.

A dynamic loading system incorporating a 22 caliber projectile was designed for load repeatability and timewise synchronization with the output from a modulated ruby laser. Using this system and a still camera, the load cycle was repeated many times to obtain photographs at different times after impact showing the stress wave in the model material. The light pulse from the laser was intense, polarized, monochromatic and of short enough duration (0.1 microseconds) to stop the rapidly propagating stress waves.

The results of this experiment indicated that the maximum dynamic stress concentration factors are independent of the time after impact at least for the time interval (50 to 140 microseconds) studied here. At a specific time after impact these factors were also found to be independent of the edge distance (a/d) and depended only on (2a/r) where a is the semi major axis of the ellipse, d is half the model width and r is the radius at the end of the major axis.

Additional information was available for calculating the stress concentrations at the top and bottom of the discontinuity and the edge

of the model adjacent to the discontinuity. These factors were generally quite small as compared to the maximum dynamic factors. The positions of the maximum and zero fringe orders were also recorded.

Using some simplifying assumptions and the one and two dimensional theory of stress wave propagation, a theoretical equation was developed which expresses the ratio of the static to the dynamic stress concentration factors as a function of poisson's ratio and the model geometry. For the material (PSM-1) used in this investigation, the difference between the theoretical and experimental $(K_s/K_d)_{T,E}$ was 5 to 10%. This equation was also compared to the experimental results of an independent investigator who studied photoelastically the problem of a dynamically loaded strut containing a circular discontinuity. For the material used (CR-39) the difference between the theoretical and experimental ratios was less than 10%.

ACKNOWLEDGMENT

I would like to express my sincere thanks to my advisor Dr. W.P.T. North for his guidance and encouragement during this investigation.

The financial support of the Defence Research Board, Grant Number 1601-33, was appreciated greatly.

In addition, I would like to express my gratitude to the Central Research Shop, especially Mr. L. Cory and Mr. D. Cox of the Electrical Division for their assistance in developing the electrical equipment.

TABLE OF CONTENTS

LIST OF FIGURES

NOMENCLATURE

A	Area, in^2
$\mathring{A}$	Angstrom unit, 10^{-8}cm.
a	Semi major axis of ellipse, in.
B	Constant
c	Velocity of propagation of longitudinal wave, in./sec.
d	Half the width of photoelastic model, in.
E	Modulus of elasticity, $lb./in^2$
F	Force, lb.
f_σ	Material fringe value, psi - in/fringe (tension)
h	Thickness of model, in.
K	Stress concentration factor
N	Fringe order
R	Constant
r	Radius of ellipse at end of major axis, in.
t	Time
u	Longitudinal displacement, in.
v	Particle velocity, in/sec.
x	Longitudinal co-ordinate, in.
α	Angular Positions of the Maximum and Zero Fringe Orders, degrees.
μ	Microseconds, 10^{-6} sec.
ν	Poisson's ratio
ρ	Mass density, lb. - sec^2/in^4
σ	Stress, lb/in^2

1. INTRODUCTION

1.1 Subject of the Investigation.

The purpose of this investigation was twofold

(a) To synchronize a modulated ruby laser as a light source in a polariscope designed to study transient stresses.

(b) To determine experimentally using this photoelastic procedure, the stress concentration factors in a strut loaded by high velocity impact and containing a symmetrically located elliptical discontinuity.

1.2 The Importance of Dynamic Stress Concentration.

A member which contains a discontinuity such as a hole, notch, or a change in cross section cannot be analysed by the elementary stress equations at least in the neighbourhood of the discontinuity.

A considerable amount of work has been done to determine static stress concentration factors for the more common discontinuities. These results have been tabulated in the form of graphs of experimental data, empirical formulae, and in some cases the more difficult form of a theoretical solution. (1)(2)(3) In the past, the effects of dynamic stress were estimated either from the results of an experiment on the member or by adding a safety factor to the static stress concentration criterion which would hopefully cope with the unknown dynamic effect.

The increasing trend toward higher performance and lower weight to strength ratios of dynamically loaded machine members has made it imperative that the phenomenon of dynamic stress concentration and distribution be well understood.

Unlike static loading, impact forces are not transmitted immediately

or invariably to all parts of the member. Thus, the deformations and corresponding stresses propagate through the member in the form of stress waves. Because of the resulting unknown variables dynamic stress concentration is not easily analysed.

1.3 Plan of Treatment.

In this investigation a photoelastic analysis employing a modulated ruby laser light source coupled to a repeatable dynamic loading system was synchronized to photograph stress wave propagation in high modulus photoelastic models. The photographic records of the isochromatic fringes were stored on a still camera by repeating the loading cycle at various intervals of time after impact.

In order to stop photographically the rapidly propagating stress waves (wave front velocity 63000 inches per second) the fast light shutter action of the modulated (Q-spoiled) ruby laser was employed to eliminate the need of a complex camera system. The laser also supplied the intense, parallel, polarized and monochromatic light, making it compatible with the photoelastic technique.

2. LITERATURE REVIEW

2.1 Static Stress Concentration.

Considerable interest has been focused on the study of static stress concentration factors. Coker and Filon (4), Neuber (5), Howland (6), Wahl and Beeuwkes (7), and Frocht (8), are just a few of the investigators who have written papers on static stress concentration. A collection of static stress concentration factors for various geometrics have been presented by Peterson (1), Roark (2), and the Engineering Science Data Unit (3). The case of an elliptical hole in a strut has been determined theoretically and experimentally in references (4) and (3).

2.2 Dynamic Stress Concentration.

The study of dynamic stress concentration is much more difficult because of the number of variables involved and the demand for sophisticated experimental equipment. In the area of dynamic photoelacticity, most investigators have turned to low modulus materials such as Hysol 8705 in which the stress wave propagation has been slowed down sufficiently so that existing equipment can be used (9)(10)(11)(12). Durelli and Dally (9) have studied the problem of a Hysol 8705 strut containing a symmetrically placed circular hole and being loaded axially by a falling weight. The hole diameter to model width was 0.29 and the dynamic stress concentration factor was 3.35 which was essentially constant with time after impact and virtually identical to the static value. The problem of a Hysol 4485 strut loaded by a falling weight and containing a semicircular discontinuity located symmetrically on opposite sides was studied by

Kumar (10). The results of this experiment indicated that the dynamic stress concentration factors were dependent on time after impact and always lower than the static values.

Unfortunately, the low modulus materials exhibit rate dependent properties. In fact, statically, the material is non-linear to the extent that it is seldom used.

In an effort to avoid these undesirable properties, several photoelastic investigations (13)(14)(15) have been carried out using conventional high modulus photoelastic materials such as Columbia Resin (CR-39) and Epoxy Resin Araldite 6020. Of these investigations, the photoelastic records have been either too poor to interpret accurately or simply records of various effects. Goldsmith and Norris (14), using the repeatability technique of loading, have obtained clear photographs of dynamic stresses in a CR-39 cantilever beam loaded on its free end by a steel sphere. Certainly, any attempts to date to record the entire event with a high speed camera have been somewhat unsatisfactory since the intensity and resolution are insufficient.

Dally and Halbleib (15) studied photoelastically the dynamic stress concentration in a CR-39 strut containing a circular hole and loaded axially by a falling weight. They used the repeatability technique and the spark gap method of lighting. This investigation showed the dynamic stress concentration factor to be independent of the time after impact, and that for a constant time after impact, the factors were dependent on the hole diameter to model width ratio. (fig. 10)

North and Taylor (16) studied photoelastically the same problem as Dally and Halbleib but used Araldite 6020 - an epoxy resin model material.

In this investigation, the ordinary light source with its many problems was replaced by a modulated ruby laser. The laser output was intense, polarized, monochromatic, and of short enought time duration (0.1 microseconds) to easily stop the rapidly propagating stress wave. The results of this experiment indicated that the dynamic stress concentration factor is dependent on the time after impact. For a constant time after impact, the factors varied linearly with the hole diameter to model widths (fig. 10).

Pao (17) suggests that the dynamic stress concentration factor depends on the impulse wave length and poisson's ratio. Since Dally and Halbleib, North and Taylor, and the author all used different materials, and impact times, the results of fig. 10 cannot be compared directly.

A comprehensive review of dynamic photoelasticity in general is given by Goldsmith (18). The detection and measurement of stress waves by other methods than a photoelastic procedure are given by Kolsky (19).

3. OUTLINE OF THE PROBLEM STUDIED

3.1 Stress Concentration Factor.

The generally accepted definition for the static stress concentration factor (K_s') in a strut under a uniform stress distribution is the ratio of the maximum stress at the discontinuity (σ_{max}) to the average stress (σ_o) at the same section.

$$K_s' = \frac{\sigma_{max}}{\sigma_o} \qquad (3\text{-}1)$$

This definition implies that an accurate measurement of the load on the member be known in order to find the average stress. For a dynamic loading condition, an accurate determination of the applied load is difficult to obtain. As a result, the definition of the average stress was assumed to be that based on the nominal section at the discontinuity when the discontinuity does not exist. For this condition, the dynamic stress concentration factor K_d is defined as

$$K_d = \frac{\sigma_{max}^d}{\sigma_{nom}^d} \qquad (3\text{-}2)$$

when σ_{max}^d is the maximum dynamic stress at the boundary of the discontinuity as a function of time after impact and σ_{nom}^d is the stress that would occur for the same time after impact and at the same position with no discontinuity present. It is not possible to compare directly the stress concentration factors K_s' and K_d as defined here. If, however, the values of K_s' are multiplied by a suitable geometric constant based

on the model width and discontinuity size, concentration factors K_s based on the gross area of the section can be obtained. The values of K_s and K_d can then be compared without difficulty. In this investigation the constant of equality between K_s and K_s' is

$$K_s = K_s' / (1-a/d) \qquad (3-3)$$

where a is the semi major axis of the ellipse and d is half the model width (see fig. 1).

3.2 Major Assumptions Involved.

1. The stress concentration factor (K_s) which is normally applied to the static loading can be considered a valid and sufficient definition for dynamic loading.

2. Since the model thickness ($\frac{1}{4}$") is small relative to the other dimensions ($1\frac{1}{2}$" wide X 8" long) it is assumed that a condition of plane stress exists. A free boundary experiences only a uniaxial state of stress having a direction tangent to the boundary. Thus, the stress optic equation for σ_{max} becomes:

$$\sigma_{max} = \frac{f_{\sigma\,max}\, N_{max}}{h} \qquad (3-4)$$

where: $f_{\sigma\,max}$ is the maximum material fringe constant psi - in/fringe.

h is the model thickness in inches

N_{max} is the maximum isochromatic fringe order at the boundary of the discontinuity.

3. At the central portion of the strut when no discontinuity is present, it is assumed that the transverse stress is negligible. Thus, the stress optic equation for σ^{d}_{nom} becomes:

$$\sigma^{d}_{nom} = \frac{f_{\sigma nom} N_{nom}}{h} \qquad (3\text{-}5)$$

where: $f_{\sigma nom}$ is the nominal material fringe constant.

N_{nom} is the nominal fringe at the axial centerline of the strut with no discontinuity present.

Combining equations 3-2, 3-4, and 3-5:

$$K_d = \frac{\sigma^{d}_{max}}{\sigma^{d}_{nom}} = \frac{f_{\sigma max} N_{max}}{f_{\sigma nom} N_{nom}} \qquad (3\text{-}6)$$

4. Although $f_{\sigma max}$ and $f_{\sigma nom}$ are probably rate dependent for the material studied here, it is assumed that the ratio of these two quantities is equal to one. Considering the work done by Dally, Durelli and Riley (20) on hysol 8705 and investigations made by Clark (21) and Frocht (22) on the high modulus materials CR-39 and Castolite respectively, this assumption probably does not lead to appreciable error in the material used here. Thus equation (3-6) reduces to:

$$K_d = \frac{\sigma^{d}_{max}}{\sigma^{d}_{nom}} = \frac{N_{max}}{N_{nom}} \qquad (3\text{-}7)$$

5. Elastic stress conditions exist for all the configurations tested. (appendix A)

6. A dynamic state of stress exists. To obtain this the longitudinal stress wave pulse must be short relative to the model length if a

quasi-static state of stress is to be eliminated. However, to maintain a plane stress condition, the stress pulse must be long relative to the model thickness. (17)(23)

3.3 The Geometric Configurations Tested

A total of sixteen models as seen in fig. 1 with various sizes of elliptical discontinuities were tested. The dimensions of all the models were $\frac{1}{4}$" thick by $1\frac{1}{2}$" wide by 8" long. One additional model was tested without the discontinuity. This model was marked by a line across its width at the location where the discontinuity would appear. The material used was a high modulus material acquired from Photolastic Incorporated under the code number of PSM-1. See Appendix A for more details concerning this material.

4. EXPERIMENTAL ARRANGEMENT AND PROCEDURE

4.1 The Light Source.

Dynamic photoelastic investigations have been hampered primarily by the lack of an intense light source. If ordinary light is used, it must be polarized, made monochromatic (300Å band width) and stopped down at the focal plane of the collimating lens to obtain a parallel light field. Thus, only a fraction of the source intensity is usable.

In order to avoid the requirement for a complex camera system, the light must be controlled to produce a light pulse of one microsecond or less if the rapidly propagating stress waves are to be stopped photographically on a still camera. The above restrictions make conventional light sources difficult to use for dynamic photoelasticity. On the other hand, the use of a pockels cell modulated ruby laser completely overcomes the light source problem. The advantages of the ruby laser light are given below. (24)

(a) The output is polarized (100%)

(b) The light is monochromatic (6943Å band width 0.1Å).

(c) The light is parallel. (less than one degree divergence) Thus, the total output can be used.

(d) The output is intense. In this experiment several neutral filters had to be used so that the film would not be overexposed.

(e) The laser is easily modulated by means of a pockels cell to produce a light pulse of 0.1 microseconds or less, a technique termed Q-spoiling.

The above characteristics make the laser compatible with

dynamic photoelasticity. Appendix B and C contain a more complete description of the laser, its operation and associated equipment.

4.2 The Integrated System of Components to Record the Birefringence.

The conventional polariscope used in this system was modified by changing the quarter-wave plates to make it compatible with the red (6943Å) laser light. Since the laser output is polarized, the polarizer of the polariscope could be omitted.

A loading mechanism incorporating a 22 caliber air pistol was designed to load the model with a repeatable, short, time duration impact load. The load duration was 30 microseconds or less which is compatible with assumption 6 of section 3.2. The pistol charging gas (nitrogen) was stored in a welder's tank and released to the gun by a pressure reducing regulator which was preset to 500 psig.

After the pellet is fired, it first activates a photocell. The resulting electrical pulse, which is amplified and delayed, triggers the laser power supply releasing energy to the laser head flash tube. When the pellet reaches the top of the model, it activates a mechanical trigger by forcing a strong spring returned steel plunger into contact with the steel model cap. This contact action simultaneously loads the model and triggers the multiple pulse hold-off circuit and pockels cell delay circuit. The output pulse from the pockels cell delay circuit cuts the half wave bias voltage off the laser head pockels cell at a predetermined time after impact. Immediately, thereafter, a short pulse of laser light (0.1 microseconds duration) passes through the polariscope and model into the open still camera.

A block diagram of the experimental apparatus is shown in fig. 2, while fig. 3 shows the laboratory arrangement. See Appendix B and C for a more complete description of the equipment and its operation.

4.3 The Data Recorded.

The first part of the problem was to determine how the maximum dynamic stress concentration factor depended on the time after impact. To do this, a model without a discontinuity and a representative model with a discontinuity was tested to determine the nominal and maximum fringe orders respectively at approximately 10 microsecond intervals between limits of 50 and 140 microseconds after impact. The results of this test plotted in fig. 7 indicate the dynamic stress concentration factors are essentially independent of the time after impact.

The second part of the problem was to determine the dynamic stress concentration factors for the various sizes of discontinuities. Since K_d is independent of time after impact, a time of 100 microseconds was used and was chosen on the basis of the maximum number of fringes that could be counted accurately considering the severest geometry tested and the resolution of the photographs. The photographs of both tests gave additional information concerning the stresses at the top and bottom of the discontinuity as well as the stress at the edge of the model adjacent to the discontinuity. The position of the maximum and zero fringe order locations on the discontinuity were also recorded.

5. RESULTS AND DISCUSSION OF THE ANALYSIS

5.1 Birefringence Photographs.

5.1.1 Fringe Propagation in Models with Time after Impact: Figure 4 is a typical selection of photographs showing the propagating stress wave identified by the isochromatic fringes at various times after impact. A line across the model without a discontinuity marks the position along which the major axis of the discontinuity would appear. The top 0.275 inches of the models across their widths is covered by the metal cap; thus, the top edge of the models where the stress is initiated cannot be seen. Near the loading point, the state of stress is biaxial; but at the centerline of the model the uniaxial state of stress assumption is approached. Furthermore, fig. 7 indicates that K_d is essentially constant over the time interval considered which indicates that the assumption of a negligible transverse stress at the model centerline is justified.

The time of impact is 30 microseconds or less (appendix C) and the wave front velocity (zero fringe order) is 63000 inches per second (appendix A). Thus, the length of the stress wave pulse is 1.9 inches. For a model length of 8 inches and a model thickness of $\frac{1}{4}$ inch, this stress pulse length obviously satisfies assumption 6 of section 3.2.

5.1.2 Fringe formation about Discontinuities at 100 microseconds after Impact: Figure 5 shows a typical set of discontinuities tested for a constant a/d of 0.58. For a particular photograph shown in this figure, there were at least two other photographs taken and the average fringe count for the three photographs was used in the analysis. The resolution of all the photographs was good and washout of the higher order

fringes was negligible which is probably due to the highly monochromatic laser light.

Figure 6 shows a typical set of discontinuities for a constant $2a/r = 2$. The maximum fringe order is nearly the same for each photograph regardless of the edge distance.

5.2 Graphical Interpretation of the Birefringence.

5.2.1 The Maximum Dynamic Stress Concentration Factor as a Function of Time after Impact: Figure 7 is a graph of the fringe order against time after impact. Curve N_{max} represents the maximum fringe order at the end of the major axis for the constant geometry indicated. The fringe count at both ends of the major axis was noted and the average of the two values was plotted. The N_{nom} curve was plotted from the information of fig. 18 shown in appendix A. The dynamic stress concentration factor K_d is the ratio of N_{max} to N_{nom} for any given time after impact. Inset in fig. 7 is K_d plotted against time and shows K_d to be relatively constant over the time interval considered. The remainder of the tests were then taken at 100 microseconds after impact based on this figure and the fact that N_{nom} was reliable for this time.

5.2.2 The Maximum Dynamic Stress Concentration Factor at a Constant Time after Impact: Figure 8 is a graph of the maximum dynamic stress factor K_d against $2a/r$ for various ratios of a/d and at a constant time after impact of 100 microseconds. The value of $N_{nom} = 2.25$ was determined from fig. 7. The experimental static stress concentration factors shown here for comparison purposes were taken from reference (3). This reference indicated that the curves were an approximate solution for three different shapes of discontinuities. One of these discontinuities was the ellipse

although, unfortunately, it was not clear which shape was actually tested and plotted.

The dynamic stress concentration factors K_d, unlike the static factors, are independent of a/d. Although this was not expected, it may be explained by considering the effect of a discontinuity on the propagating stress wave. At the upper boundary of the discontinuity, a fraction of the incident compression wave is reflected as a tension wave from the free boundary and this fraction tends to increase as a/d or a increases (d = 0.75" is constant).

Consider a constant value of a/d approximately equal to 0.42 where the dynamic factors K_d are approximately equal to the static factors K_s. If 2a/r increases, r must decrease and a decreasing r is associated with an increase in stress concentration which is consistent with fig. 8.

If 2a/r is constant and a/d is allowed to increase, the net section decreases but the net section sees less of the incident stress wave. Thus, the increase in average stress across the net section is reduced and this reduced average stress would tend to lower the stress concentration factor. But, as a increases, then r must also increase if 2a/r is to remain constant and an increasing r is associated with a decrease of stress concentration. The two effects of an increasing r and an increasing stress wave reflection due to an increasing a combine to reduce the stress concentration factor K_d to the point where it is independent of a/d. This same argument can also be applied to the case when 2a/r is constant and a/d is reduced below the value of a/d = 0.42. In this case, the net result is to increase K_d beyond the value of K_s in such a way that

K_d is still independent of a/d.

Figure 9 is a graph of the experimental $(K_s / K_d)_E$ against 2a/r for various values of a/d. The graph indicates that K_s varies from a maximum of 1.84 K_d at a/d = 0.75 to a minimum of 0.89 K_d at a/d = 0.25. At a/d = 0.42, K_s is approximately equal to K_d.

Figure 10 shows a graph of K_d against a/d for circular discontinuities (2a/r = 2). The author's curve, the static curve, and the results obtained by other investigators are indicated.

5.2.3 The Dynamic Stress Concentration Factors at the Top and Bottom of the Discontinuity: The dynamic stress concentrations associated with the top and bottom of the discontinuity were also determined. These results were obtained for a constant model geometry (a/d = 0.58; 2a/r = 5.6) and various times after impact as well as a constant time after impact (100 microseconds) and various model geometries. The plotted data is represented in fig. 11 and fig. 12 respectively. Figure 11 indicates that K_t and K_b increase with time after impact. These curves could not be plotted for times after 120 microseconds because N_{nom} was not clearly defined beyond this time. Figure 12 shows that K_t and K_b vary with 2a/r and also a/d. K_t is always higher than K_b except for the case of the smallest discontinuity where K_t appears to equal K_b. This is likely due to the length of the propagating wave front; that is, it envelopes the smallest discontinuity completely.

5.2.4 The Dynamic Stress Concentration Factors at the Edge of the Model Adjacent to the Discontinuity: Figure 11 shows K_e for a constant geometry and various times after impact. The fringe order N_e at the edge of the model was small and not greater than two. Thus, it was difficult

to determine N_e accurately since the best fringe count estimates were generally not better than the nearest half order.

Figure 13 shows K_e at 100 microseconds after impact for various model geometries. This graph indicates that K_e depends on both a/d and 2a/r; but, at a/d = 0.42 to 0.25, K_e appears to be nearly independent of 2a/r. That is, as the discontinuity becomes small, its influence on the wave front at the edge of the model becomes less pronounced, indeed, for the smallest discontinuity the trend is to indicate no effect at all ($K_e = 1$).

5.2.5 The Angular Position of the Maximum and Zero Fringe Orders: The angular positions of the maximum and zero fringe orders on the boundary of the hole for a constant model geometry are plotted in fig. 14 as a function of time. The maximum stress occurs initially at some point removed from the net section and as time increases the maximum fringe order moves toward the net section.

This figure also shows the zero fringe order positions above and below the centerline of the discontinuity. The zero position in both cases tends to move toward the net section as time increases.

Figure 15 shows the zero fringe order positions on the upper boundary of the discontinuity against 2a/r at a constant time after impact (100 microseconds) for the geometries studied. These curves indicate that the position of N = 0 depends on both a/d and 2a/r. The N = 0 positions on the lower boundary of the hole were quite similar.

5.3 Estimate of the Experimental Error.

This estimate is confined to the error in the maximum dynamic stress concentration factor (K_d) at 100 microseconds after impact. Errors in load repeatability and the repeatability of the time after impact are

included in the measurement of the fringe orders.

Considering the severest geometry tested, each photograph showed a fringe count of about 16 fringes for N_{max}. It is possible for the error in this figure to approach $\pm$ 1 fringe or $\pm$ 6%. This 6% error may be overestimated since the value of N_{max} is the average of at least three separate photographs.

The nominal fringe order obtained from fig. 7 at 100 microseconds after impact is 2.25 which is the value used to calculate K_d. The N_{nom} curve of figure 7 is based on the results of ten photographs taken at ten different times after the impact. Hence, the error in this value of N_{nom} is probably not greater than $\pm$ 0.1 fringe or $\pm$ 4.5%.

Since K_d is equal to the ratio N_{max} / N_{nom} then the error in K_d is about $\pm$ 10%.

5.4 Theoretical Considerations.

Using some simplifying assumptions and the one and two dimensional theory of stress wave propagation, an equation can be developed which shows the relationship between the incident and transmitted longitudinal waves in a strut which has a change in cross section.

Consider a strut as shown in the sketch which is assumed to be very long. That is, the assumption is made that the ends of the strut are far enough away from the change in cross section so that reflections from the ends do not interfere with the initial stress pulse. Further assumed, is a uniformly distributed compressive stress pulse that is long with respect to the discontinuity and suddenly applied to the free end.

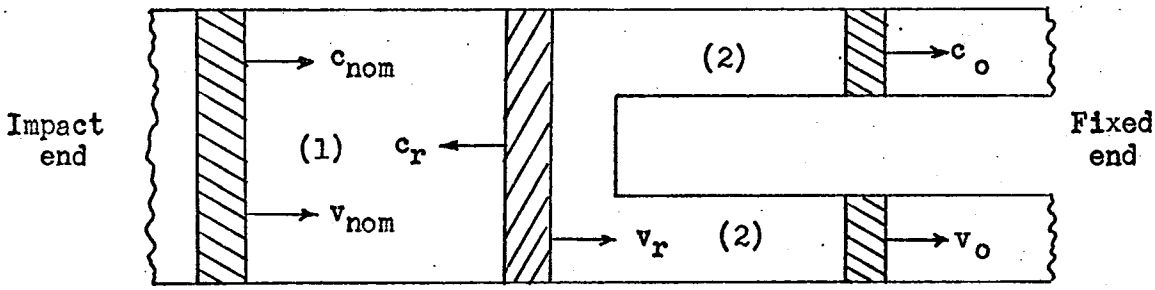

The conditions of continuity at the change in cross section require that

$$F_1 = F_2 \qquad (5\text{-}1)$$

$$v_1 = v_2 \qquad (5\text{-}2)$$

where F is the force and v is the particle velocity. Let σ_{nom}, σ_r, and σ_o be the stress in the incident, reflected and transmitted pulse respectively. From equation (5-1) and (5-2)

$$A_1 (\sigma_{nom} + \sigma_r) = (\sigma_o) A_2 \qquad (5\text{-}3)$$

$$v_{nom} - v_r = v_o \qquad (5\text{-}4)$$

From the elementary theory of wave propagation (25)(26)

$$\sigma = \rho c v \qquad (5\text{-}5)$$

where ρ is the mass density of the bar, and c is the wave velocity (Appendix A). Solving equation (5-3)(5-4) and (5-5) gives

$$\sigma_o = \frac{2A_1 \rho_2 c_o}{A_1 \rho_1 c_{nom} + A_2 \rho_2 c_o} \cdot \sigma_{nom} \qquad (5\text{-}6)$$

$$\sigma_r = \frac{A_2 \rho_2 c_o - A_1 \rho_1 c_{nom}}{A_1 \rho_1 c_{nom} + A_2 \rho_2 c_o} \cdot \sigma_{nom} \qquad (5\text{-}7)$$

If the assumption is made that the velocity c_o at the net section of a strut containing an elliptical or circular hole is better represented by the two dimensional plane wave propagation theory, then c_o is given by the dilational wave equation.

$$c_o = \sqrt{\frac{E_2(1-\nu)}{(1+\nu)(1-2\nu)\rho_2}}$$

Furthermore, if the simplifying assumptions of $\rho_1 = \rho_2$, $E_1 = E_2$ and poisson's ratio (ν) is not rate dependent are made and since $c_{nom} = \sqrt{E_1/\rho_1}$ then,

$$\frac{c_{nom}}{c_o} = \sqrt{\frac{(1+\nu)(1-2\nu)}{(1-\nu)}} = R \text{ (constant)} \qquad (5\text{-}8)$$

Substituting equation (5-8) into (5-6) yields

$$\frac{\sigma_{nom}}{\sigma_o} = \frac{A_1 R + A_2}{2A_1} = B \text{ (constant)} \qquad (5\text{-}9)$$

Using equation (5-9) and the equation for the dynamic stress concentration factor we have

$$K_d = \frac{\sigma_{max}}{\sigma_{nom}} = \frac{\sigma_o}{\sigma_{nom}} \cdot \frac{\sigma_{max}}{\sigma_o} = \frac{K_s'}{B} \qquad (5\text{-}10)$$

where σ_{max} is the stress at the ends of the major axis of the ellipse and the ratio of σ_{max} to the transmitted mean stress σ_o is assumed to be

equal to the static stress concentration factor K_s' based on the net section. Since K_s' is equal to K_s multiplied by the ratio of the net area to the gross area then (5-10) after substitution for B becomes

$$\frac{K_s}{K_d} = \frac{A_1 R + A_2}{2A_2} \qquad (5\text{-}11)$$

Substituting for A_1 and A_2 in terms of the geometric properties of the strut, the theoretical equation (5-11) becomes

$$\left(\frac{K_s}{K_d}\right)_T = \frac{R + (1 - a/d)}{2\,(1 - a/d)} \qquad (5\text{-}12)$$

Equation (5-12) indicates that the ratio of the static to the dynamic stress concentration factor depends only on a/d and poisson's ratio.

For a given a/d, the value of K_s depends primarily on the radius (r) at the end of the major axis of the ellipse and is not too sensitive to the curvature of the upper and lower boundaries of the ellipse. Although the value of K_d for any a/d depends on r, it is also dependent on the proportion of stress wave reflection at the discontinuity. This stress wave reflection is primarily a function of a/d and increases as a/d increases. Within limits, the curvature of the upper and lower boundary of the discontinuity does not affect the proportion of the incident wave reflected.

The result of these effects is that the ratio K_s to K_d tends to be independent of the radius r and becomes primarily a function of a/d. This can be seen experimentally from fig. 9. In this figure at

a/d = 0.75, r varies from 1/16" to 9/16" but K_s / K_d is nearly invariant in the change in r.

Figure 16 is a graph of the theoretical and experimental $(K_s / K_d)_{T,E}$ against a/d ($\nu = 0.38$). For a particular value of a/d, the experimental point plotted represents the average $(K_s / K_d)_E$ for the four models tested. This graph indicates that equation (5-12) is in very good agreement with the experimental $(K_s / K_d)_E$; the theoretical values being 5% to 10% higher than the experimental values.

The experimental results of Dally and Halbleib (15) who tested only circular discontinuities are also plotted in fig. 16. The theoretical results of their experiments also shown, vary from those of this investigation largely because poisson's ratio for their model material was 0.42 or approximately 10% higher. Their experimental results also fit this proposed theoretical solution very nicely.

6. RECOMMENDATIONS

6.1 Suggestions for Experimental Improvement.

In this experiment, the maximum duration of impact was not greater than 30 microseconds. This was determined by measuring the electrical contact period and it is quite probable that the duration of impact was considerably shorter than this. Therefore, a measurement of the actual pulse duration and the associated load variation would be of interest. It would make experimental procedures more versatile if this load time pulse could be changed in both magnitude and time.

The nominal fringe orders and thus the nominal stresses were somewhat difficult to analyse. It would be helpful if another method could be used to verify the nominal stresses. This might be done by using a very fast response strain gauge.

6.2 Suggestions for Further Work.

1. Accurate measurements should be carried out to determine the stress optic coefficients and the modulus of elasticity over a wide range of strain rates to definitely establish the effect of strain rate on these quantities.

2. It has been recognized that dynamic stress concentration depends on poisson's ratio and the pulse length (17). Hence, investigations should be carried out with these two quantities as parameters.

3. Since the ruby laser supplies a very intense short duration light pulse, the extension of dynamic photoelasticity to the three dimensional analysis using the scattered light technique is advisable. Probably more important is the use of holography in three dimensional dynamic

photoelastic investigations.

4. It would be of interest to study the difference between the static and dynamic stress concentration for the same configurations tested here but with the ellipse oriented 90 degrees so that its major axis is parallel to the longitudinal axis of the strut. In this case, the deviation between K_s and K_d measured at the end of the minor axis may be a minimum.

5. The static stress concentration factors from reference (3) are obviously wrong for various values of a/d at 2a/r = 2 (circular holes) indicating that these factors are likely in error for other values of 2a/r. Therefore, these values should be checked out experimentally.

7. CONCLUSIONS

1. The nominal fringe orders propagate in the model with different but constant velocities. These velocities range from 63,000 inches per second for the zero fringe order to 54,500 inches per second for the first third order fringe encountered.

2. The maximum dynamic stress concentration factor K_d was found to be essentially constant with time for the interval 50 to 140 microseconds after impact.

3. At 100 microseconds after impact, the maximum dynamic stress concentration factors are independent of the ratio a/d and depend only on the ratio 2a/r. When a/d is approximately 0.42, the dynamic and static stress concentration factors are approximately equal. As a/d increases beyond the value 0.42, the deviation between K_s and K_d increases and K_s is always higher than K_d with a maximum difference of 45.6% based on K_s at a/d = 0.75. As a/d decreases below the value of 0.42, the deviation between K_s and K_d again increases; but now K_s is always less than K_d with a maximum difference of 12.2% based on K_s at a/d = 0.25.

4. The isochromatic fringe photographs provided additional information about the stress concentrations at the top and bottom of the discontinuities and the stress concentrations at the edge of the models adjacent to the discontinuities. These stress concentrations were generally quite small as compared to the values of K_d. The positions of the maximum and zero fringe orders were also obtained and were plotted as additional information.

5. The static modulus of elasticity E for this material is 340,000 lb./in.^{2} and the rate dependent dynamic modulus was calculated as 440,000 lb./in.^{2} This represents an increase of 29.5% (Appendix A).

6. The objective of incorporating a modulated ruby laser as the light source in dynamic photoelasticity was accomplished. The advantages of the ruby laser are as follows:

(a) The very intense short duration Q-spoiled pulse is monochromatic, polarized, and parallel. Obviously then, the laser is an ideal light source for dynamic photoelasticity.

(b) The intensity of this laser was tremendous. Even though the light pulse was only 0.1 microseconds or less in duration, several neutral density filters had to be used to prevent overexposure of the film. This is in contrast to the use of conventional light sources where every precaution is used to minimize the loss of intensity.

(c) The resolution of the photographs was very good. This can be attributed to the high degree of monochromaticity and the very short duration of the output pulse.

There are some disadvantages associated with the use of the laser. These are as follows:

(a) The wavelength of the output being near the infrared decreases the material fringe sensitivity by 21%.

(b) To obtain good contrast, Polaroid infrared film type 413 had to be used. The standard Polaroid film type 47 3000ASA was not sensitive enough to the laser output and only limited success was obtained with this film.

(c) Some focusing problems were encountered since an ordinary light

source had to be used. The use of a gas laser for this purpose would have been ideal.

(d) The output of the laser is hazardous to the human eye. Hence, it is important that the output not be viewed directly or as reflected from a good reflecting surface. There are additional personal hazards in that the pockels cell power supply maintains a bias of 12,000 volts while the laser maintains some 1,400 volts.

With due respect to the disadvantage (d), the other disadvantages are far outweighed by the advantages.

7. The agreement between the theoretical and experimental K_s / K_d is very good and therefore certainly noteworthy. The versatility of this equation is encouraging since it fits very well the results of an independent investigator who used a different pulse length and a different photoelastic material.

8. BIBLIOGRAPHY

1. Peterson, R.E. Stress Concentration Design Factors, New York: John Wiley & Sons Inc.
2. Roark, R.J. Formulas for Stress and Strain, McGraw-Hill Inc. 1965.
3. Engineering Science Data Unit, Stress Concentration Data, No. 65004, London: Engineering Science Data Unit, Inst. Mech. Engrs., 1965.
4. Coker, E.G. and Filon, L.N.G., Photoelasticity, Cambridge University Press, 1931.
5. Neuber, H. "Theory of Notch Stresses: Principles of Exact Stress Calculations, "Julius Springer, Berlin, 1937.
   Translated by F.A. Raven, D. Taylor, Model Basin, Washington, D.C., Nov. 1945.
6. Howland, R.C.J. "On the Stresses in the Neighborhood of a Circular Hole in a Strip Under Tension," Philosophical Transactions of the Royal Society of London, Series A, Vol. 229, 1930.
7. Wahl, A.M. and Beeuwkes, R. "Stress Concentration Produced by Holes and Notches," Trans. A.S.M.E, Vol. 56, 1934, p. 617-625.
8. Frocht, M.M. "Factors of Stress Concentration Photoelastically Determined," Journal of Applied Mechanics, Trans. A.S.M.E, Vol. 57, 1935, p. A 67.
9. Durelli, A.J. and Dally, J.W. "Stress Concentration Factors under Dynamic Loading Conditions," Journal of Mechanical Engineering Science, Vol. 1, (No. 1, 1957,) p. 1-5.
10. Kumar, S. "Transient Stress Concentration," M.A. Sc. Thesis, University of Windsor, 1967.

11. Karvata, K. and Hashimoto, S. "On Some Differences between Dynamic and Static Stress Distributions," Experimental Mechanics, February 1967, p. 91-96.

12. Kuske, A. "Photoelastic Research on Dynamic Stresses," Experimental Mechanics, Vol. 6, (No. 2, Feb. 1966), p. 105-112.

13. Williams, M.L., Jessey, M.E. and Parmerter, R.R. "Some Exploratory Photoelastic Studies in Stress Wave Propagation," S.E.S.A., Vol. 17, (No. 2, 1960), p. 121-134.

14. Goldsmith, W. and Norris, G.W. "Stresses in Curved Beams Due to Transverse Impact," Proc. of 3rd U.S. Nat. Cong. of App. Mech., 1958, p. 153.

15. Dally, J.W. and Hulbleib, W.F. "Dynamic Stress Concentrations at Circular Holes in Struts," Journal of Mechanical Engineering Science, March, 1965.

16. North, W.P.T. and Taylor, C.E. "Dynamic Stress Concentration Using Photoelasticity and a Laser Light Source," Experimental Mechanics, Vol. 16, (No. 7, July 1966), p. 337.

17. Pao, Y.H. "Dynamic Stress Concentration in an Elastic Plate," Journal of Applied Mechanics, Series E, Vol. 29, (No. 2, June, 1962), p. 299-305.

18. Goldsmith, W. "Dynamic Photoelasticity, Experimental Techniques in Shock and Vibration," A.S.M.E., 1962 p. 25-55.

19. Kolsky, H. "The Detection and Measurement of Stress Waves, Experimental Techniques in Shock and Vibration," A.S.M.E., p. 11-25.

20. Dally, J.W., Riley, W.F., and Durelli, A.J. "A Photoelastic Approach to Transient Stress Problems Employing Law Modulus Materials," Journal of Applied Mechanics, Vol. 26, Trans. A.S.M.E., Vol. 81, Series E, 1959, p. 613-620.

21. Clark, A.B.J. "Static and Dynamic Calibration of a Photoelastic Model Material CR - 39," S.E.S.A., Vol. 14, (No. 1, 1956), p. 195-204.

22. Frocht, M.M. International Symposium on Stress Wave Propagation in Materials, Interscience Publishers Inc., New York, 1960, p. 111.

23. Christie, D.G. "Reflection of Elastic Waves from a Free Boundary," Philosophical Magazine, Vol. 46, 1955, p. 527-541.

24. North, W.P.T. "A Laser Light Source in Dynamic Photoelasticity," "Thesis prepared at the University of Illinois, Department of Theoretical and Applied Mechanics, Urbana, Illinois, 1965.

25. Ripperger, E.A. and Abramson, H.N. "Reflection and Transmission of Elastic Pulses in a Bar at a Discontinuity in Cross Section," Proc. 3rd Mid-Western Conf. Solid Mechanics, 1957, p. 135-145.

26. Timoshenko, S.P. and Goodier, J.N. Theory of Elasticity, McGraw-Hill Inc., 1951, p. 438.

27. Shea, R. "Dynamic Stress Concentration Factors," Experimental Mechanics, Jan. 1964, p. 20-24.

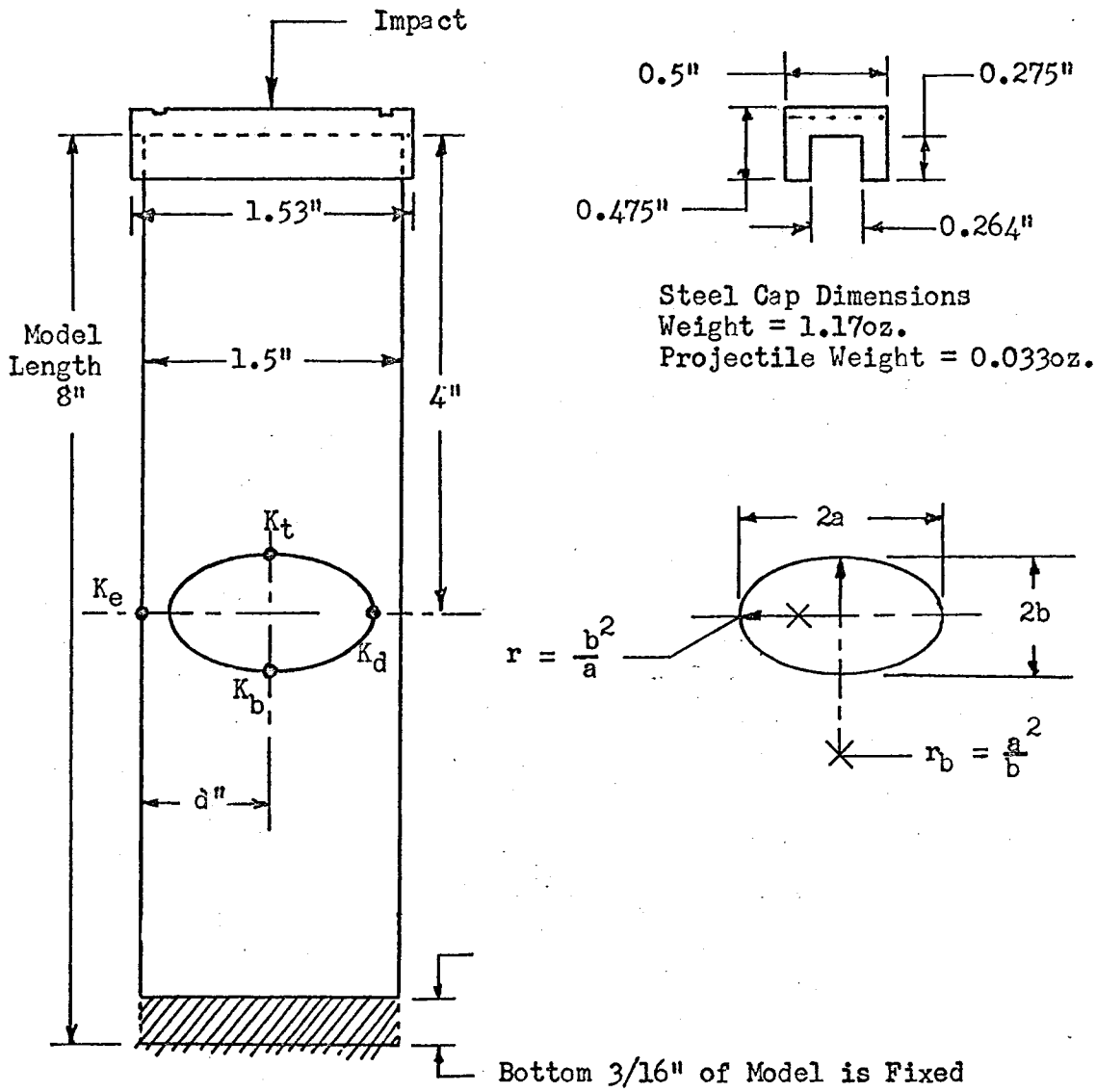

Configurations Tested									
a"	a/d	r" →				2a/r →			
9/16	0.75	1/16	3/32	3/16	a	18	12	6	2
7/16	0.58	1/16	3/32	5/32	a	14	9.33	5.6	2
5/16	0.42	1/16	3/32	5/32	a	10	6.67	4	2
3/16	0.25	1/16	3/32	1/8	a	6	4	3	2

Fig. 1 The Model Dimensions

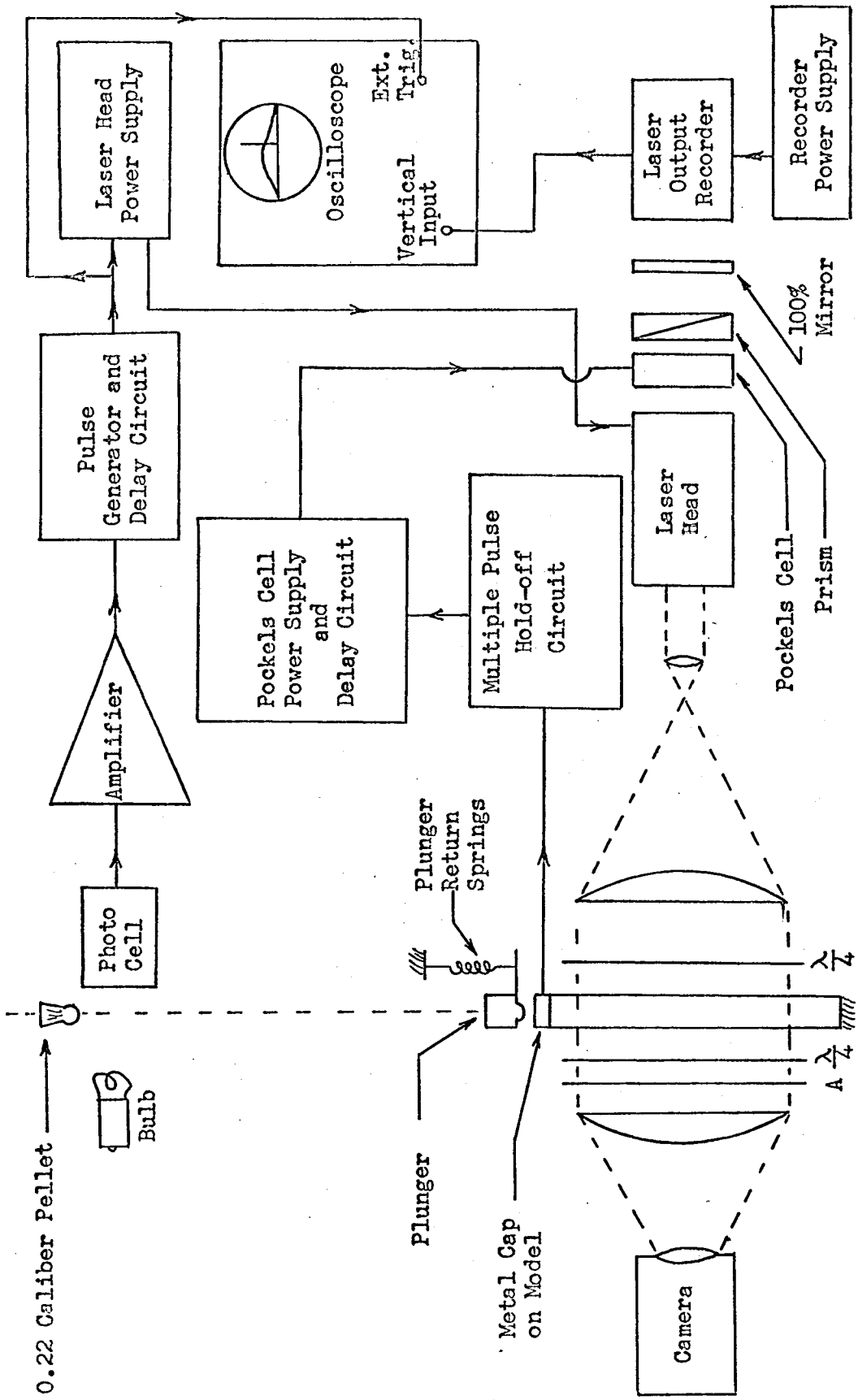

Fig. 2 Block Diagram of the Experimental Apparatus

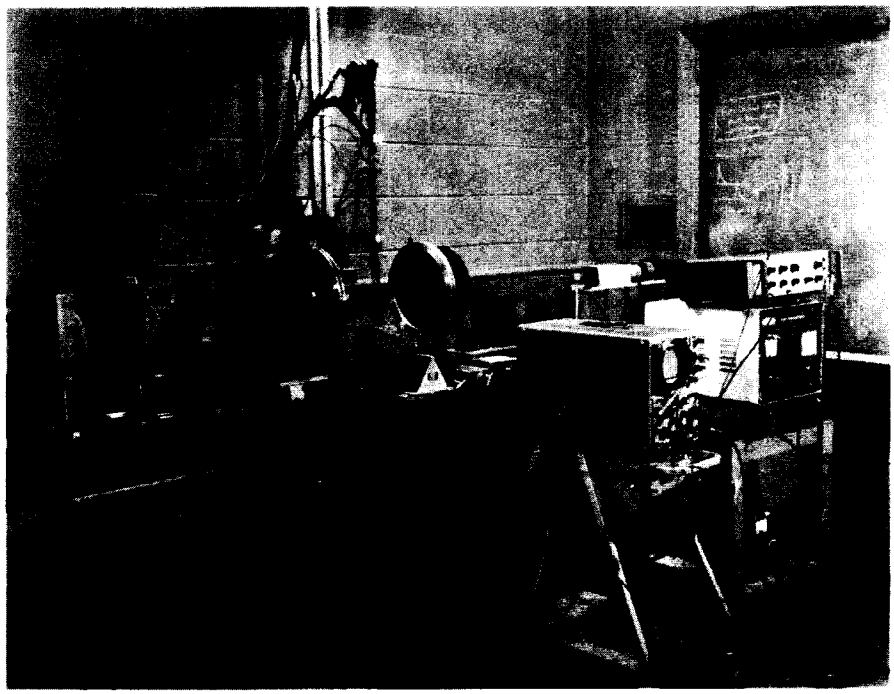

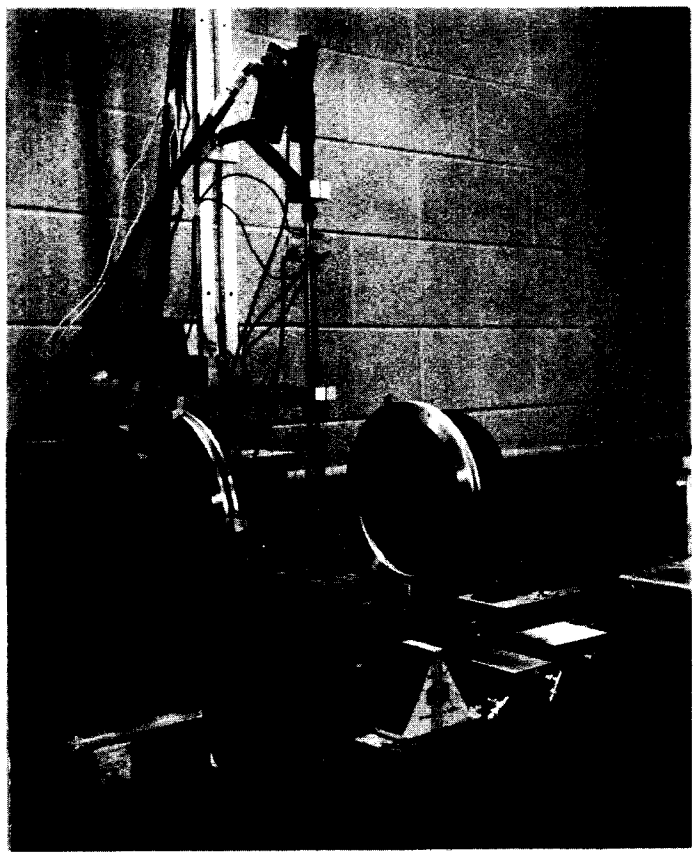

Fig. 3 Laboratory Arrangement

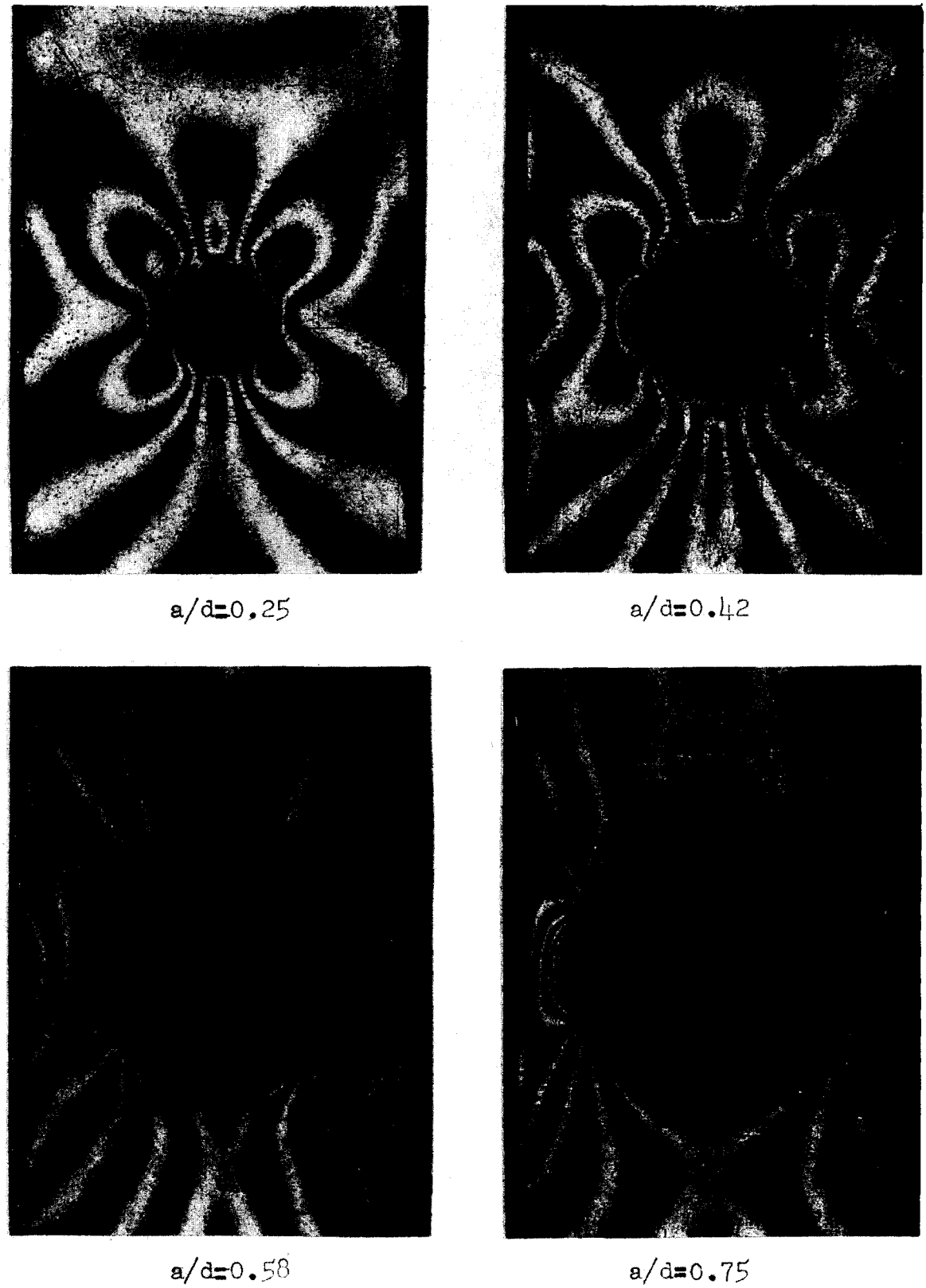

Fig. 6 Isochromatic Fringe Pattern about Discontinuities for 2a/r=2 and Time after Impact of 100μSeconds

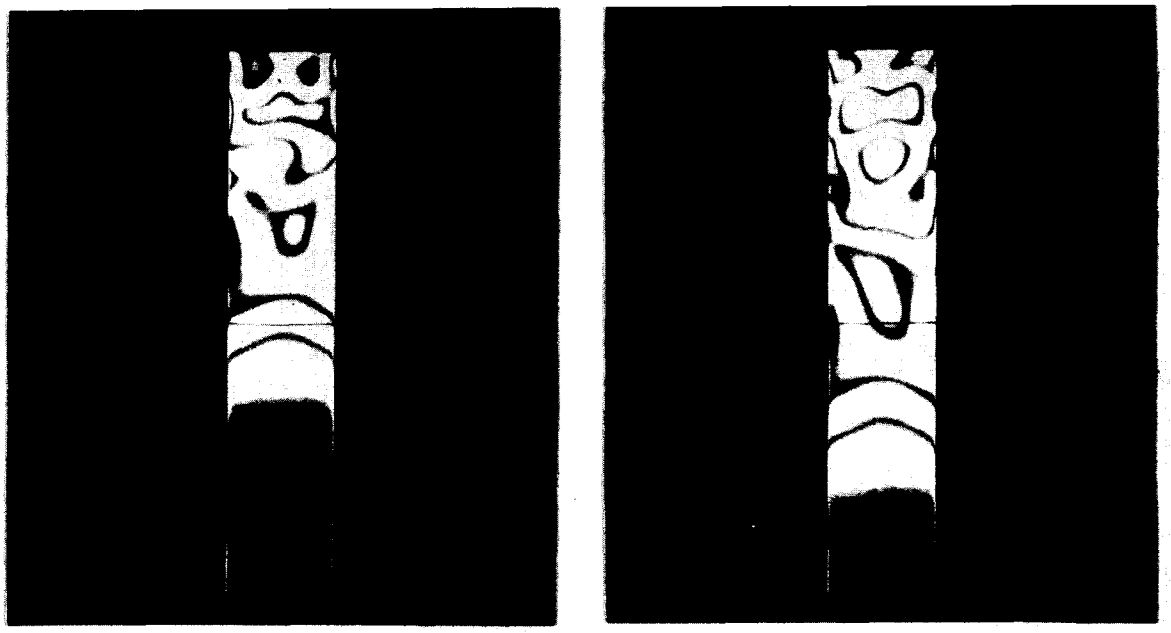

90μsec. 110μsec.

Nominal Fringe Photographs

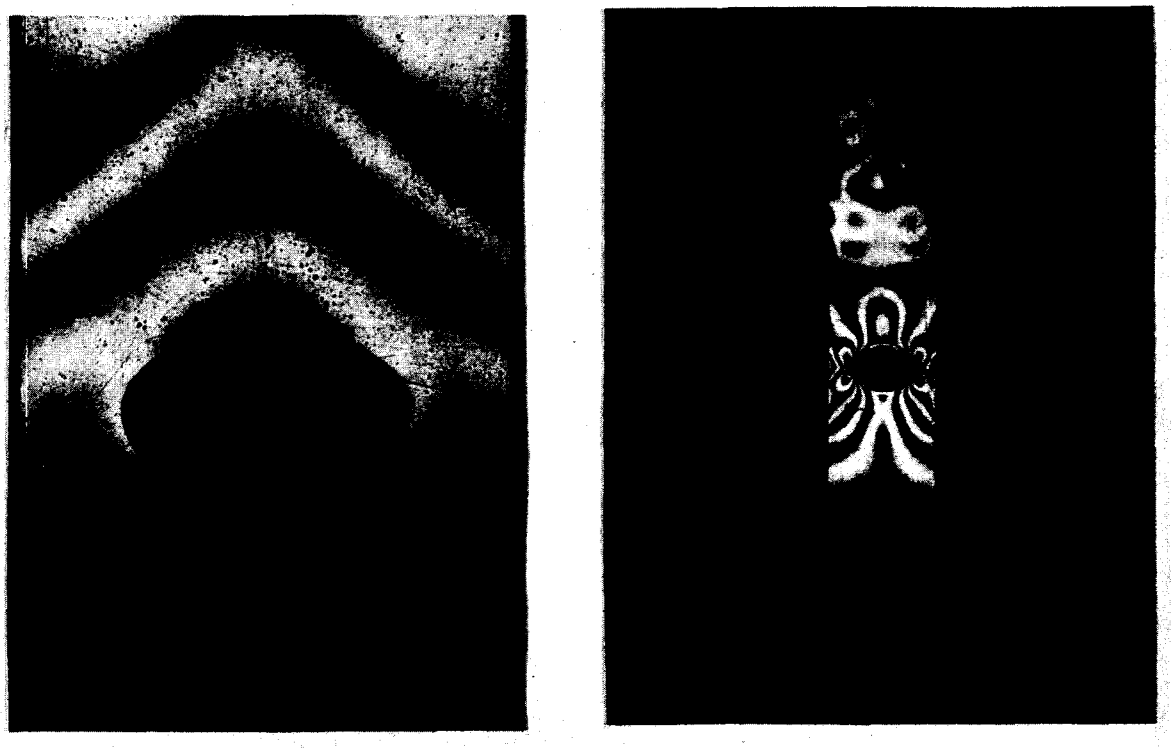

70μsec. 96μsec.

a/d=0.58, 2a/r=5.6

Fig. 4 Isochromatic Fringe Propagation with Time after Impact

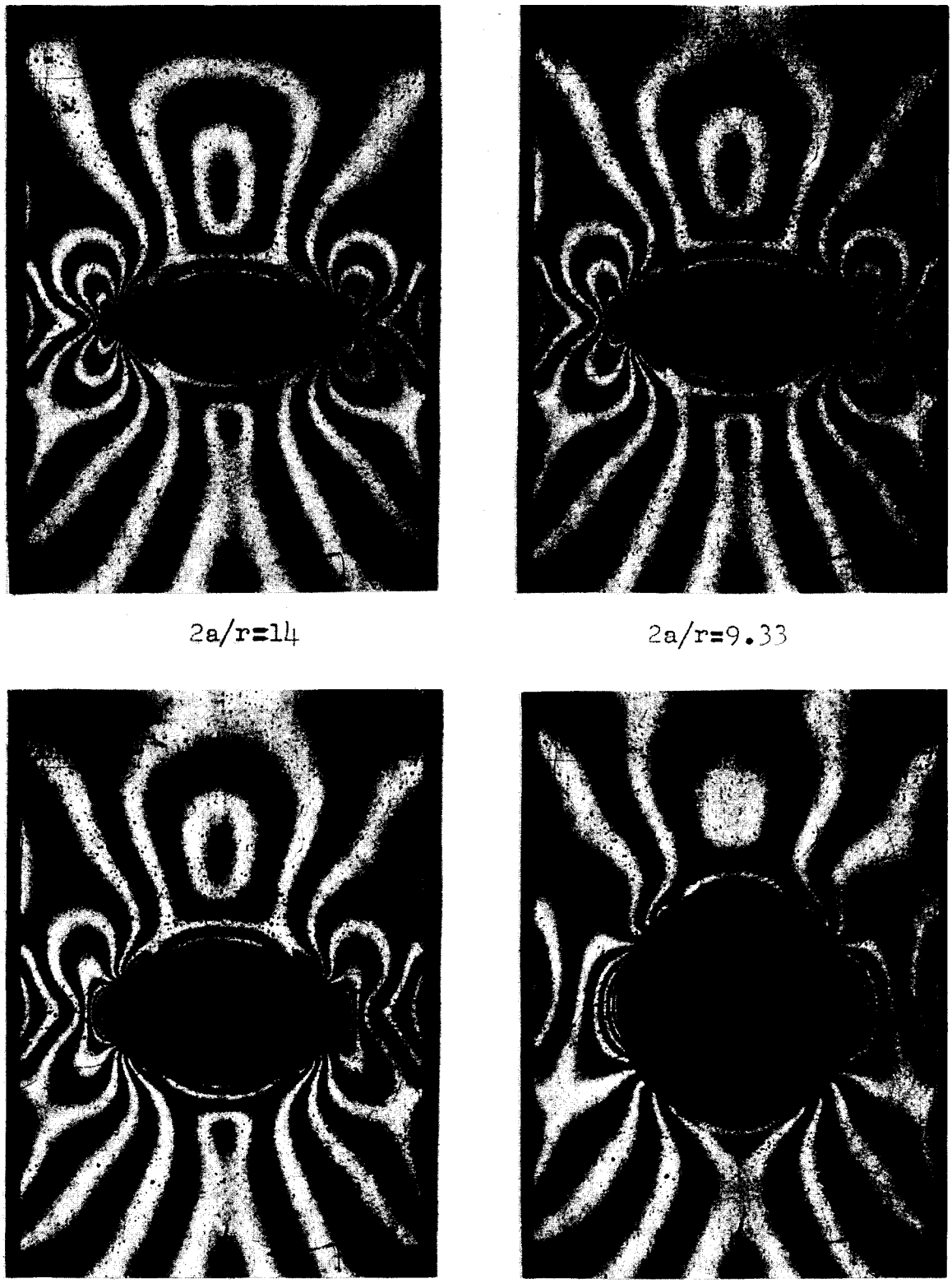

2a/r=14 2a/r=9.33

2a/r=5.6 2a/r=2

Fig. 5 Isochromatic Fringe Pattern about Discontinuities for a/d=0.58 and Time after Impact of 100μSeconds

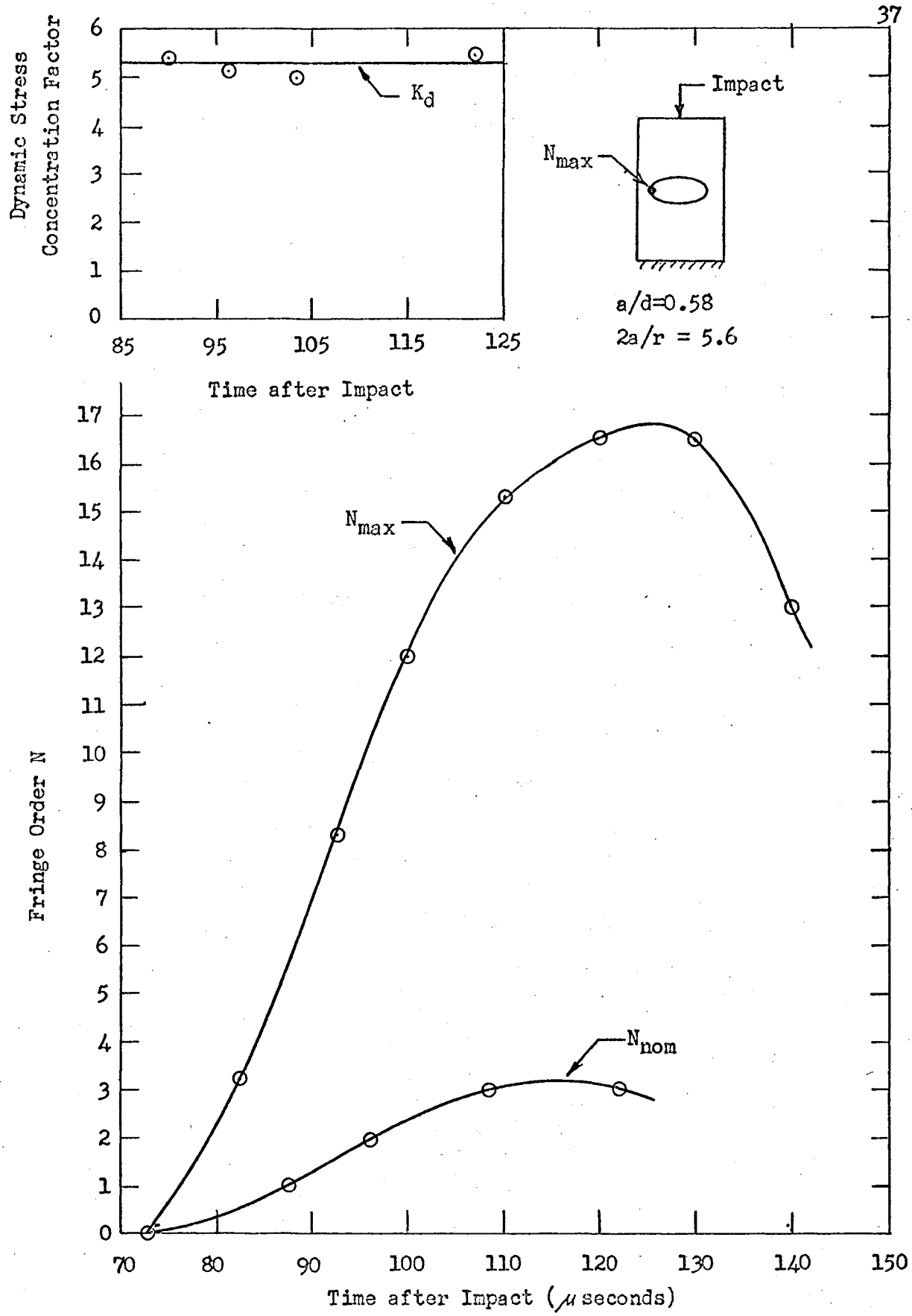

Fig. 7 Maximum Dynamic Stress Concentration Factor K_d against Time after Impact

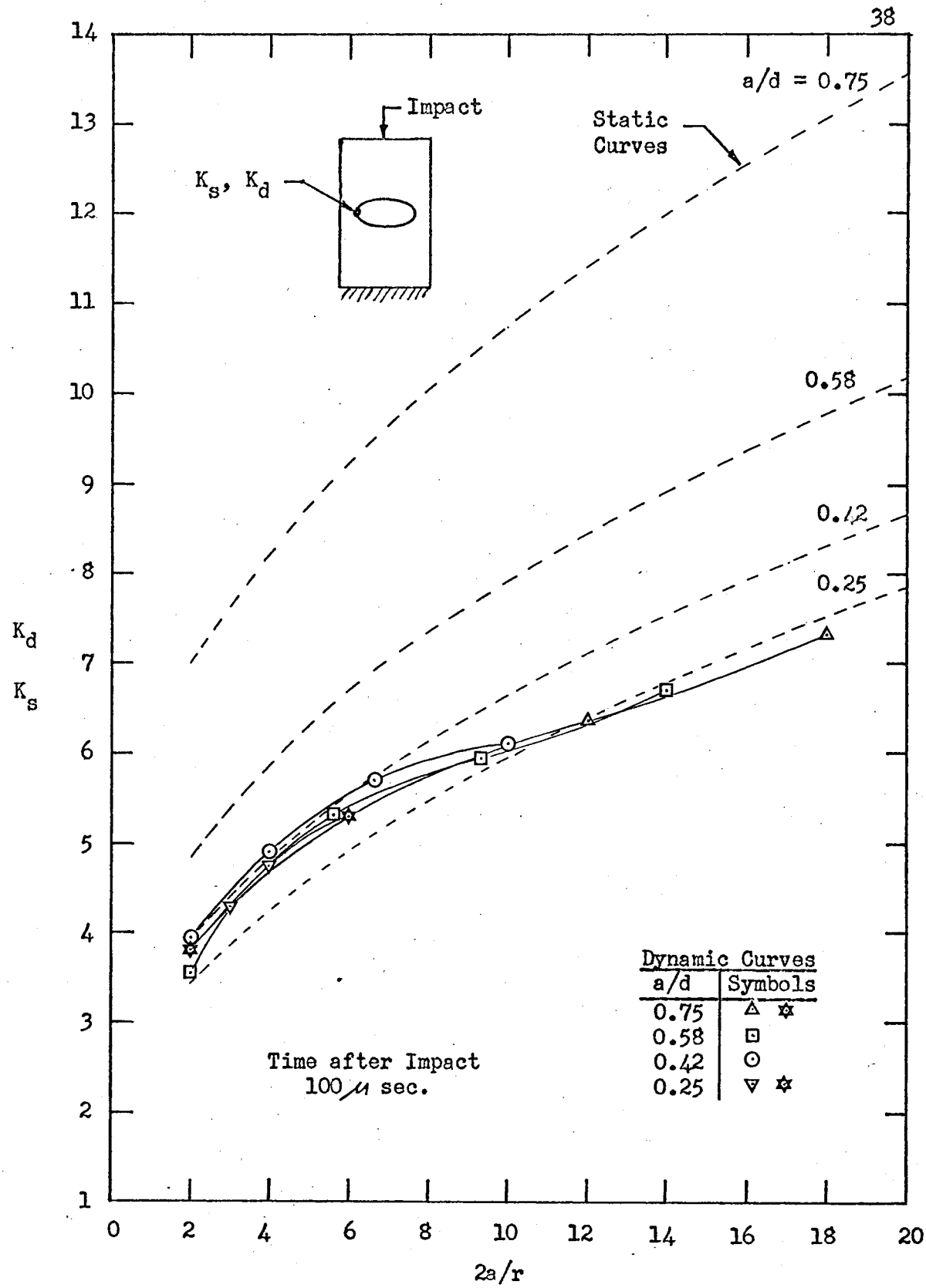

Fig. 8 Maximum Dynamic and Static Stress Concentration Factors against (2a/r) for various (a/d) ratios

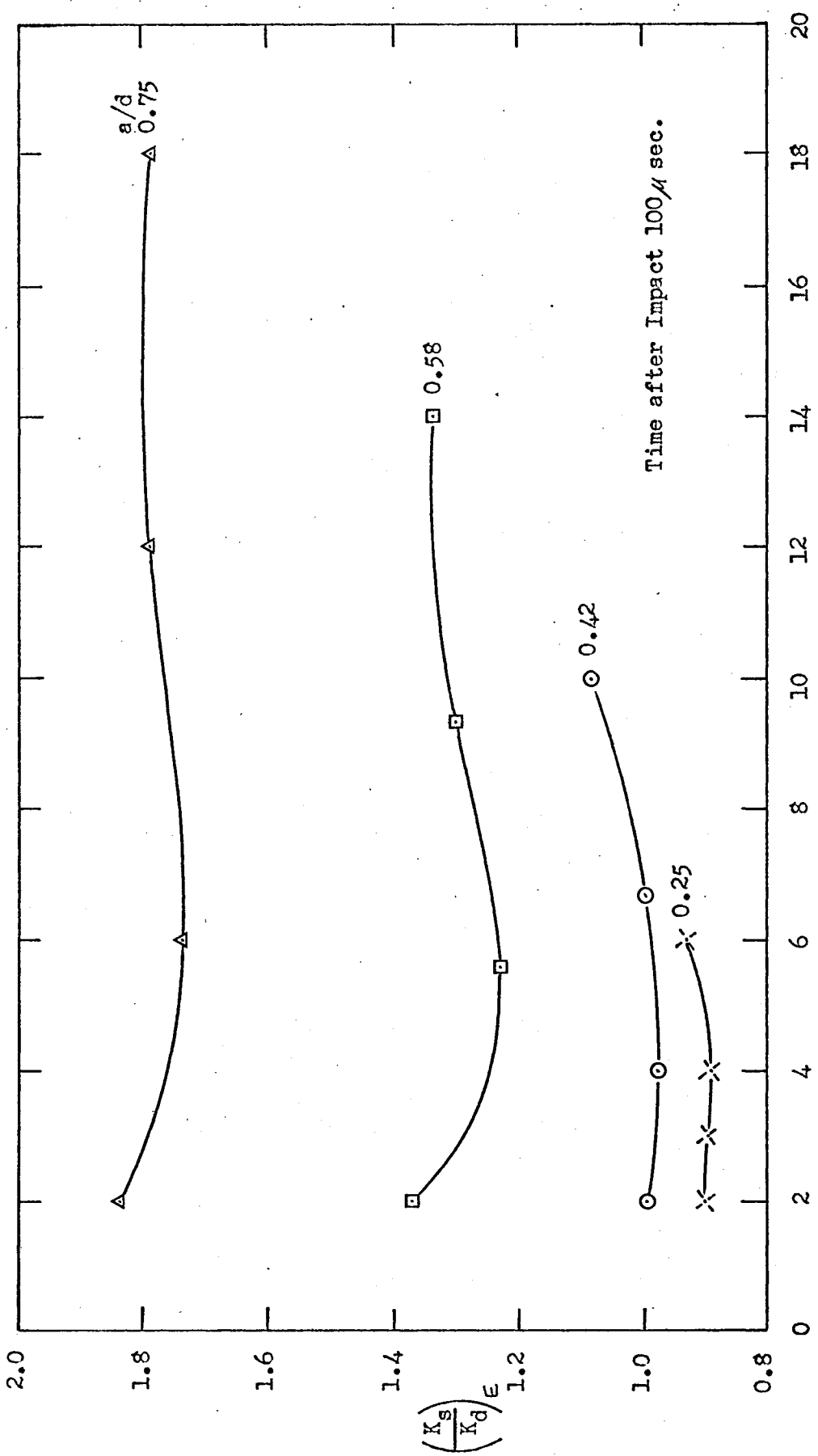

Fig. 9 Ratio of the Static to Dynamic Factors against (2a/r) for various (a/d) ratios

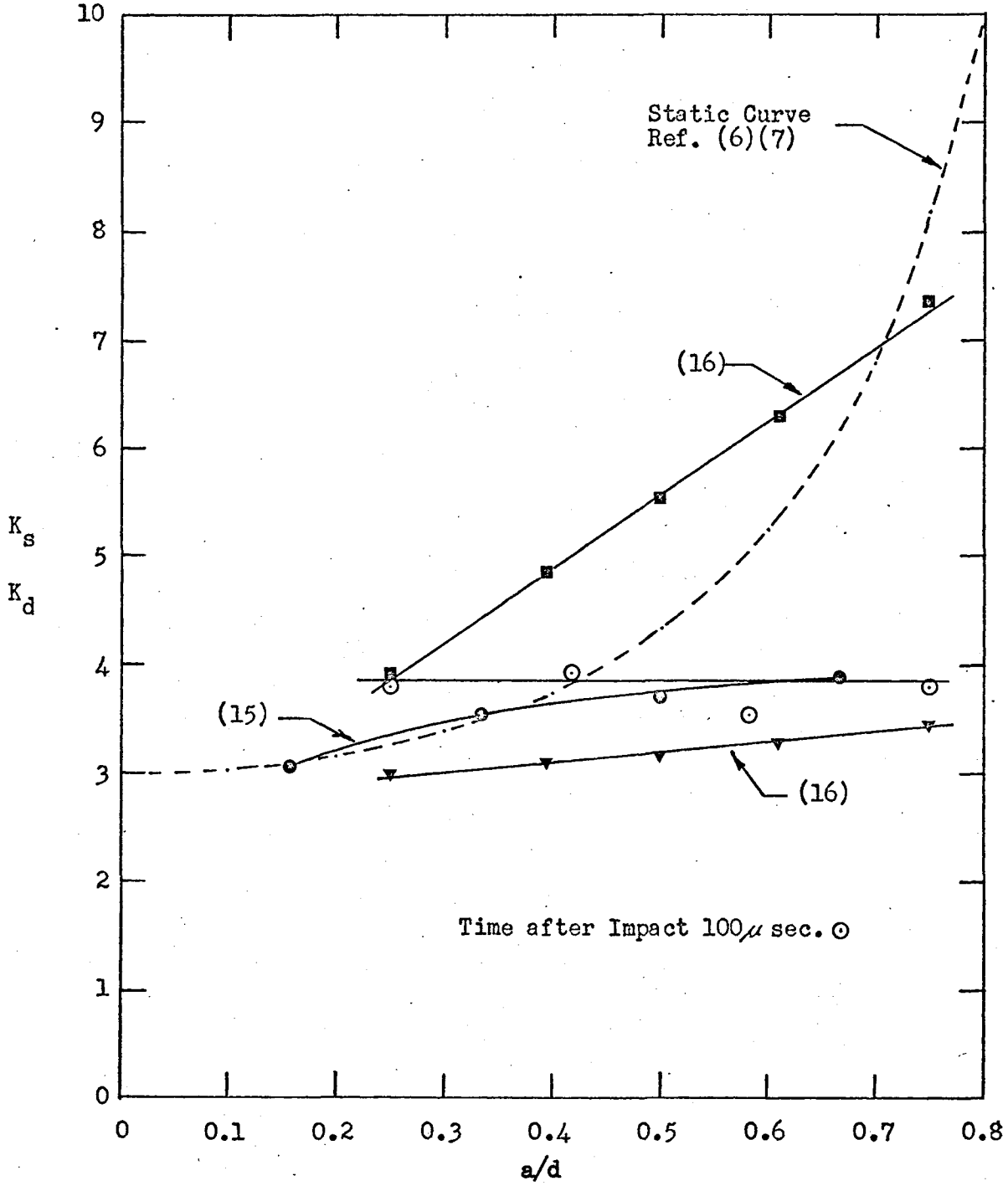

Fig. 10 Dynamic and Static Stress Concentration Factors as a Function of a/d for Circular Holes (2a/r = 2)

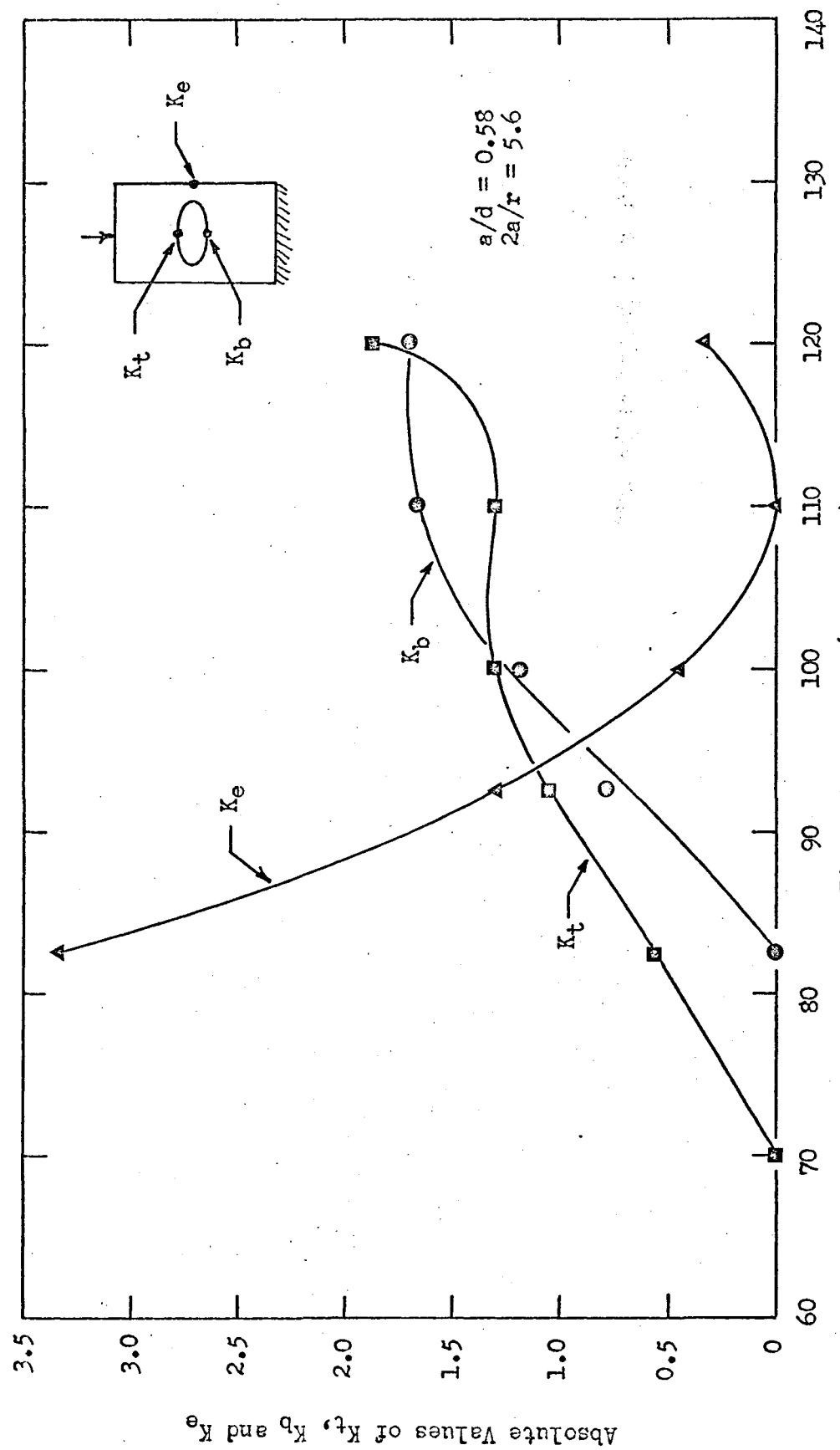

Fig. 11 Dynamic Stress Concentration Factors K_t, K_b and K_e against Time after Impact

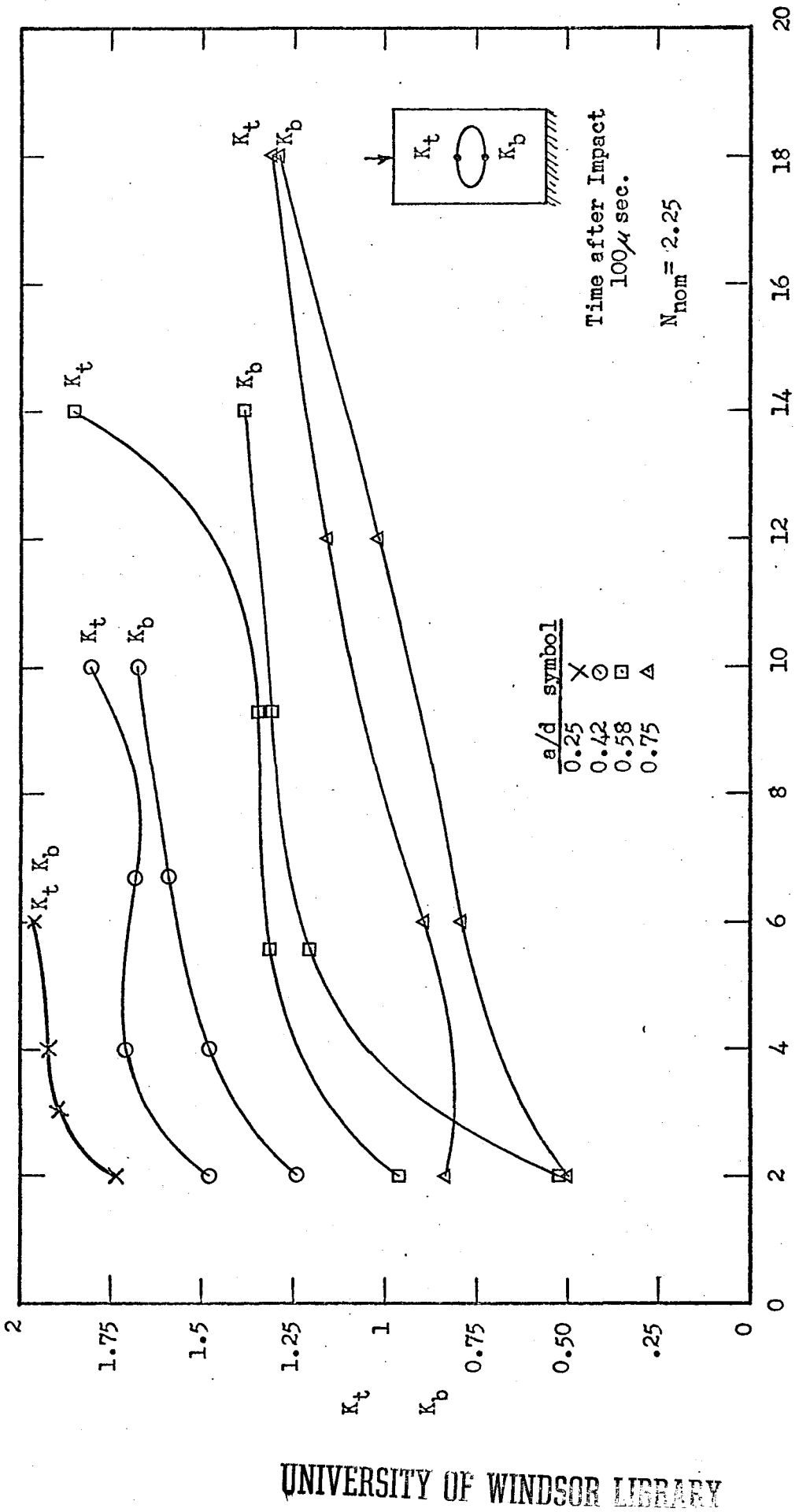

Fig. 12 Dynamic Stress Concentration Factors

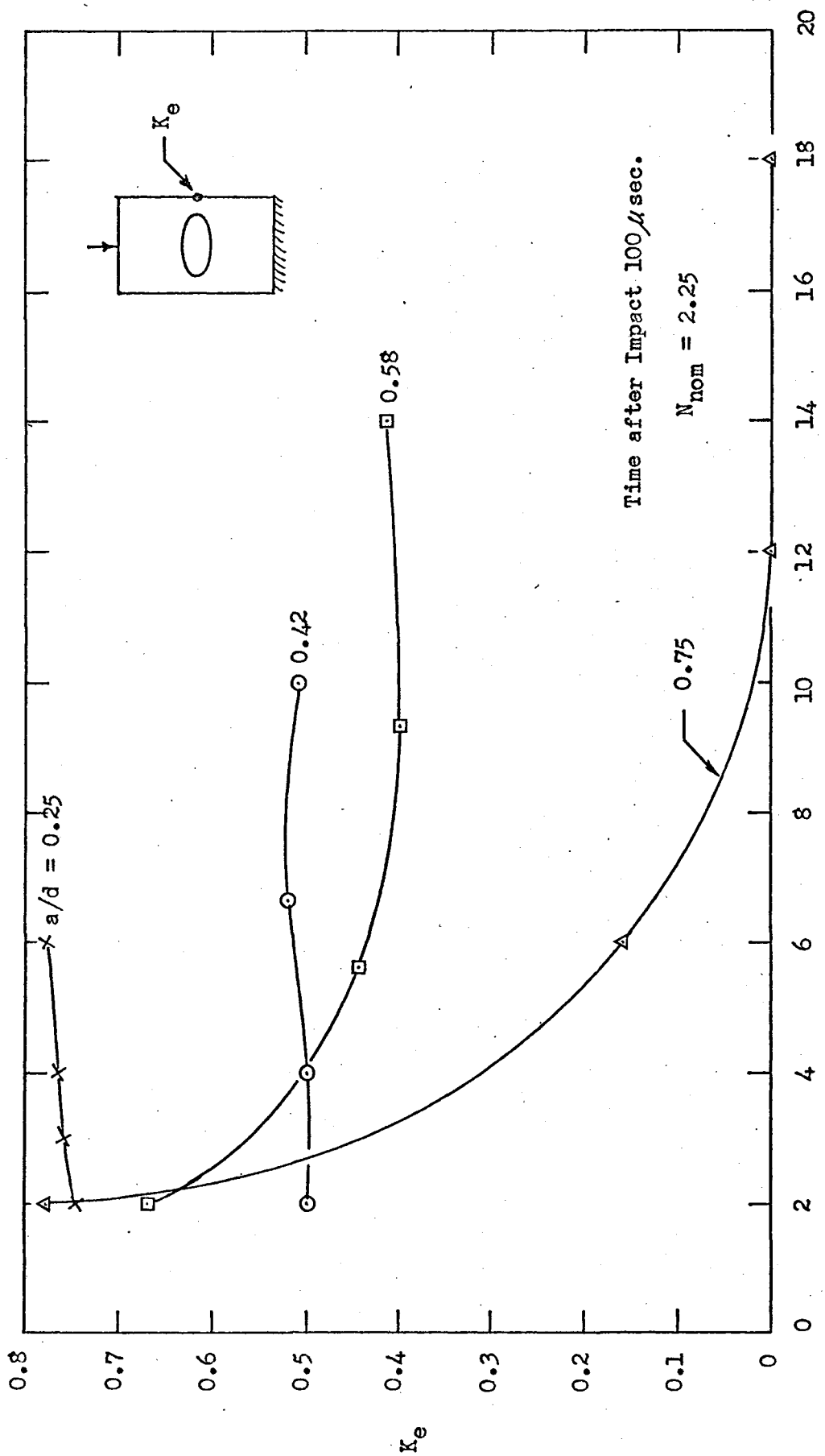

Fig. 13 Dynamic Stress Concentration Factor K_e against 2a/r

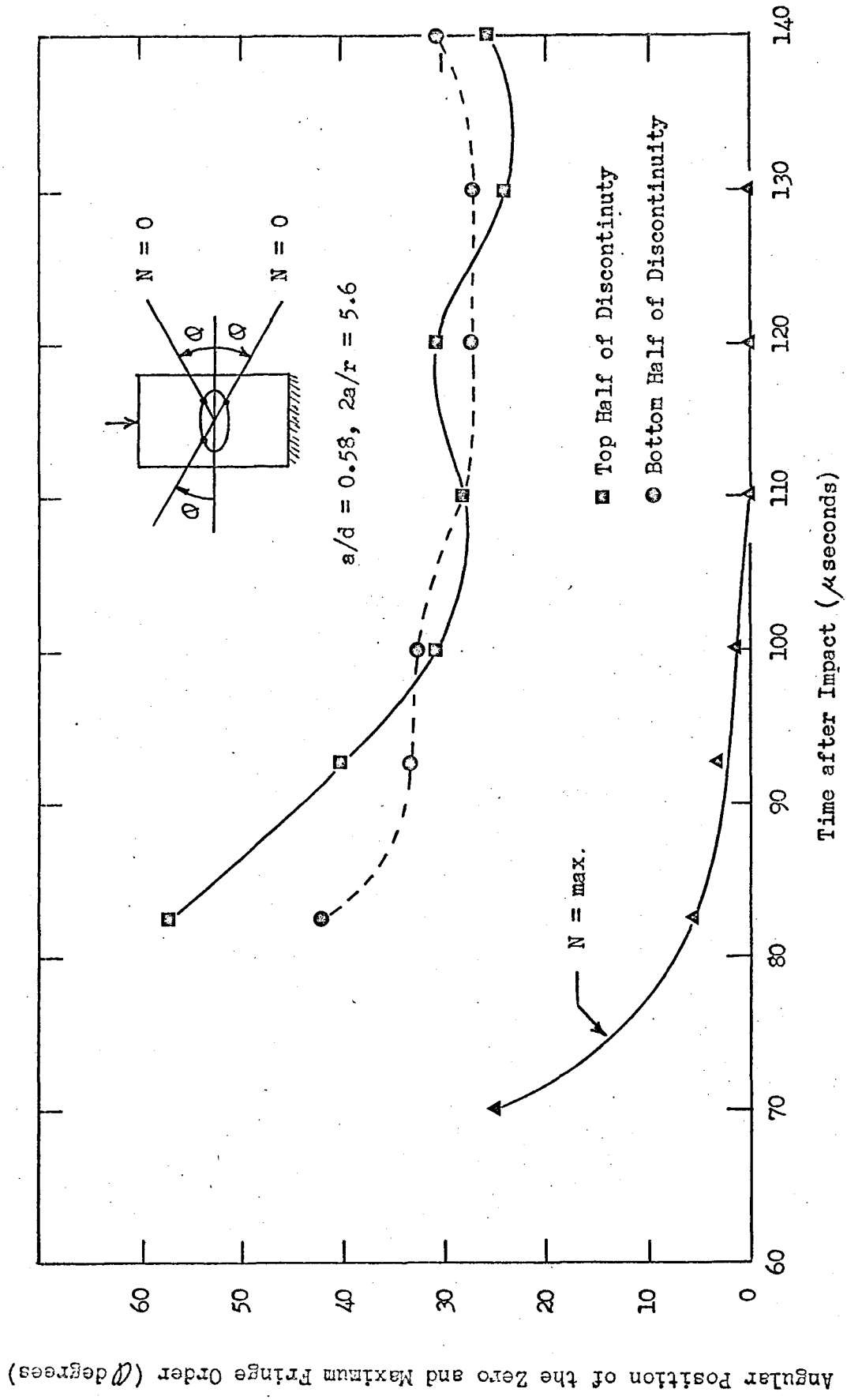

Fig. 14 Zero and Maximum Fringe Order Positions against Time after Impact

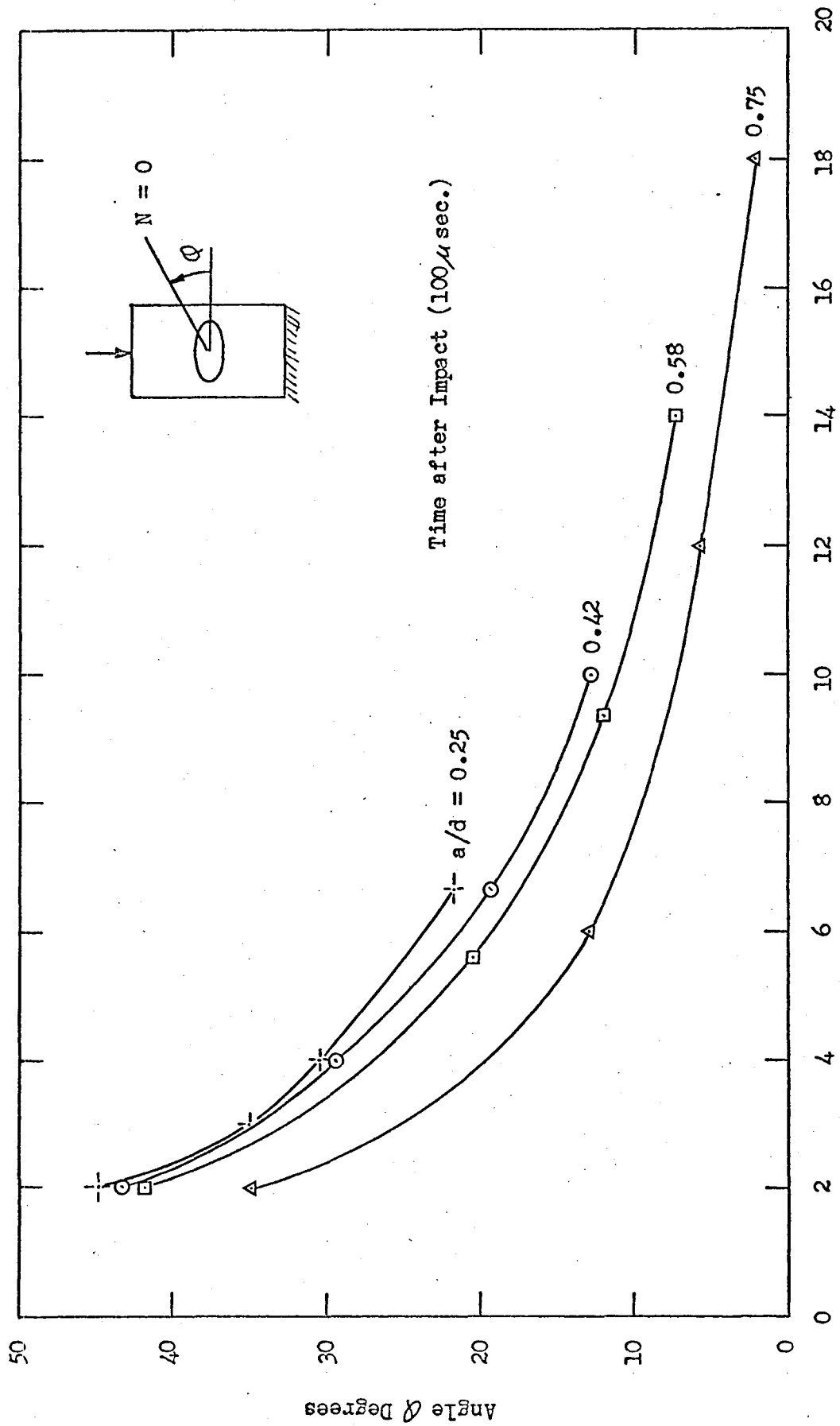

Fig. 15 Zero Fringe Order Positions on Upper Boundary of Discontinuity against (2a/r)

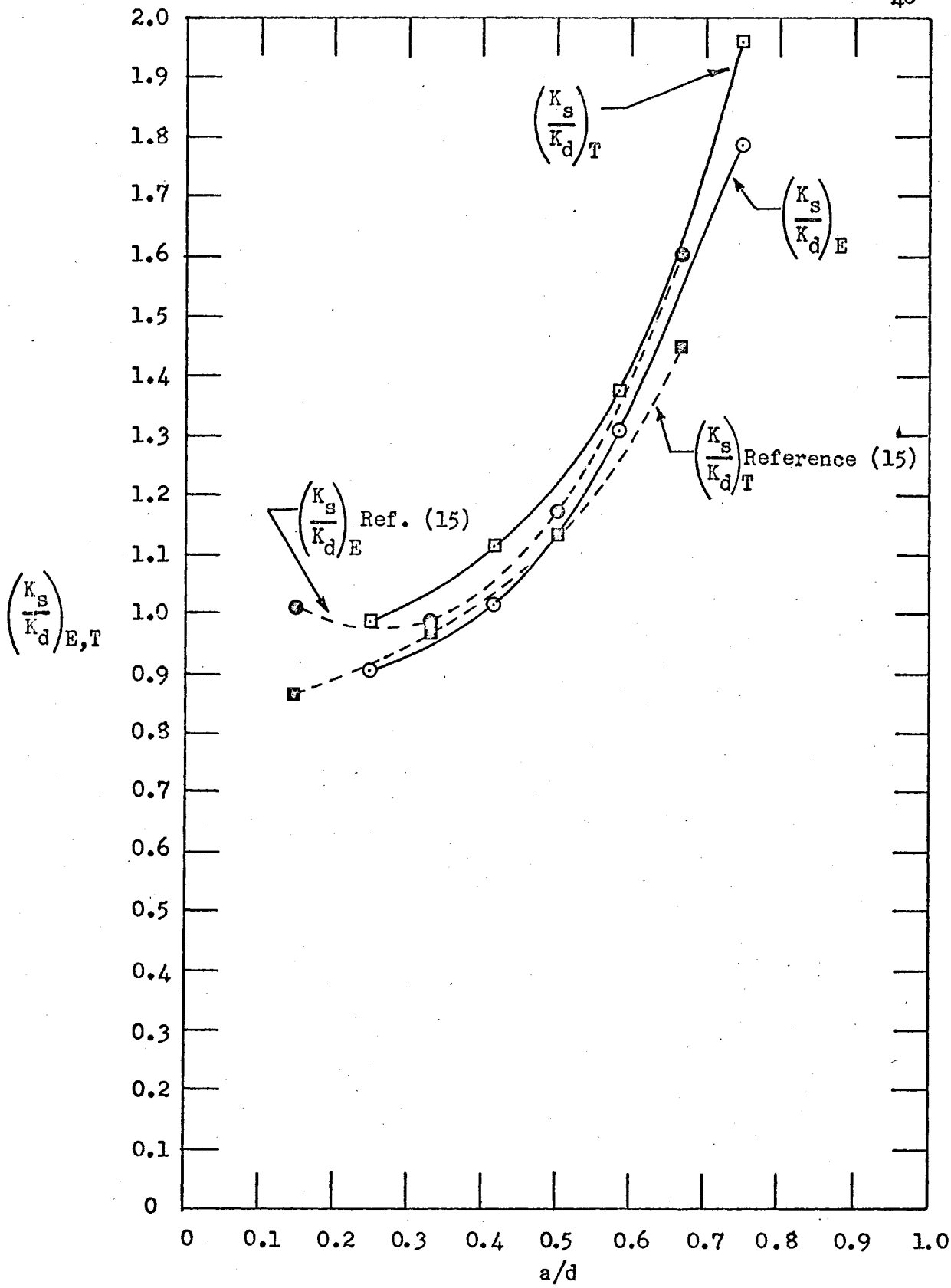

Fig. 16 Experimental and Theoretical Ratio of the Static to Dynamic Stress Concentration Factors against (a/d)

APPENDIX A

MATERIAL CALIBRATION

The material used here was a polyester material obtained from Photolastic Incorporated under the code number of PSM-1. The manufacturer states that the material exhibits low creep, minimum time edge effects and good machining characteristics. The listed elastic constants are:

poisson's ratio (ν) = 0.38

modulus of elasticity (E) = 340,000 lb./in^2

static material fringe constant (f_σ) = 40 psi - in./fringe (tension)

In this investigation, it was found that this material could be machined quite well without obtaining machining stresses if an ordinary two-fluted or four-fluted milling cutter was used at normal drilling speeds. The multiple flute cutter and high speed miller technique was found to be completely unsatisfactory. The resistance to time edge effects (absorption of moisture at the model boundaries producing undesirable stresses) is noteworthy since models two weeks after machining were still in good condition.

A.1 Static Calibration.

A static calibration was carried out on the PSM-1 material using a constant moment beam to determine the linearity of load versus fringe order. The results are shown in fig. 17 and indicate a very good linear relationship to a fringe order of at least fifteen. An additional point was plotted with a fringe order of approximately twenty. This point was difficult to determine with accuracy since the high fringe orders were

quite narrow and almost washed out. Thus, no attempt was made to determine the fractional fringe order at this point. From this figure, the material fringe value (static) was calculated as f_σ = 37.7 psi - in./fringe using standard green light (5461Å). If the red light of the ruby laser (6943Å) had been used, f_σ would be 47.9 psi - in./fringe.

A.2 Dynamic Calibration.

Figure 18 shows the nominal fringe order displacements measured from the photographs along the longitudinal axis of the model against time after impact. The slope of these lines which is constant gives the individual fringe order velocities when the slopes are multiplied by the model to photograph scale factor of 2.65:1. Although the zero, first, and second orders plotted very well, difficulty was encountered in trying to interpret the two third order fringes particularly at 130 and 140 microseconds after impact. These fringes tended to run together at these times.

Figure 19 is a graph of fringe order velocity against fringe order where it is obvious that as the fringe order increases the velocity decreases.

From the theory of elasticity (26), the differential equation of a longitudinal wave propagating in an elastic bar is given by:

$$\frac{\partial^2 u}{\partial t^2} = c^2 \frac{\partial^2 u}{\partial x^2} \qquad \text{(A-1)}$$

The general solution of (A-1) is:

$$u = f(x + ct) + g(x - ct) \qquad \text{(A-2)}$$

where: x is a point along the longitudinal axis of the bar measured from the impact end.

u is the displacement of this point for any time t after impact.

c is the constant longitudinal wave velocity and is a function of the modulus of elasticity E and the mass density of the bar

$$c = \sqrt{E/\rho} \qquad \text{(A-3)}$$

The mass density and wave front velocity of this material is

$$c = 63{,}000 \text{ in/sec}$$

$$\rho = 111.8 \times 10^{-6} \text{ lb. sec.}^2/\text{in}^4$$

Using equation (A-3) the dynamic modulus of elasticity can be found.

$$E_d = \rho c^2 = 440{,}000 \text{ lb/in}^2$$

Thus, E_d is 29.5% greater than the static modulus of elasticity.

No attempt was made to determine the dynamic fringe constant f_σ. The dynamic modulus of elasticity E_d is rate dependent and this is probably true of the material fringe constant f_σ. However, the stress concentration factor K_d involves the ratio $f_{\sigma_{max}}/f_{\sigma_{nom}}$ and the effect is cancelled assuming the fringe velocities about the discontinuity are not too different from the velocity at points farther removed from the discontinuity.

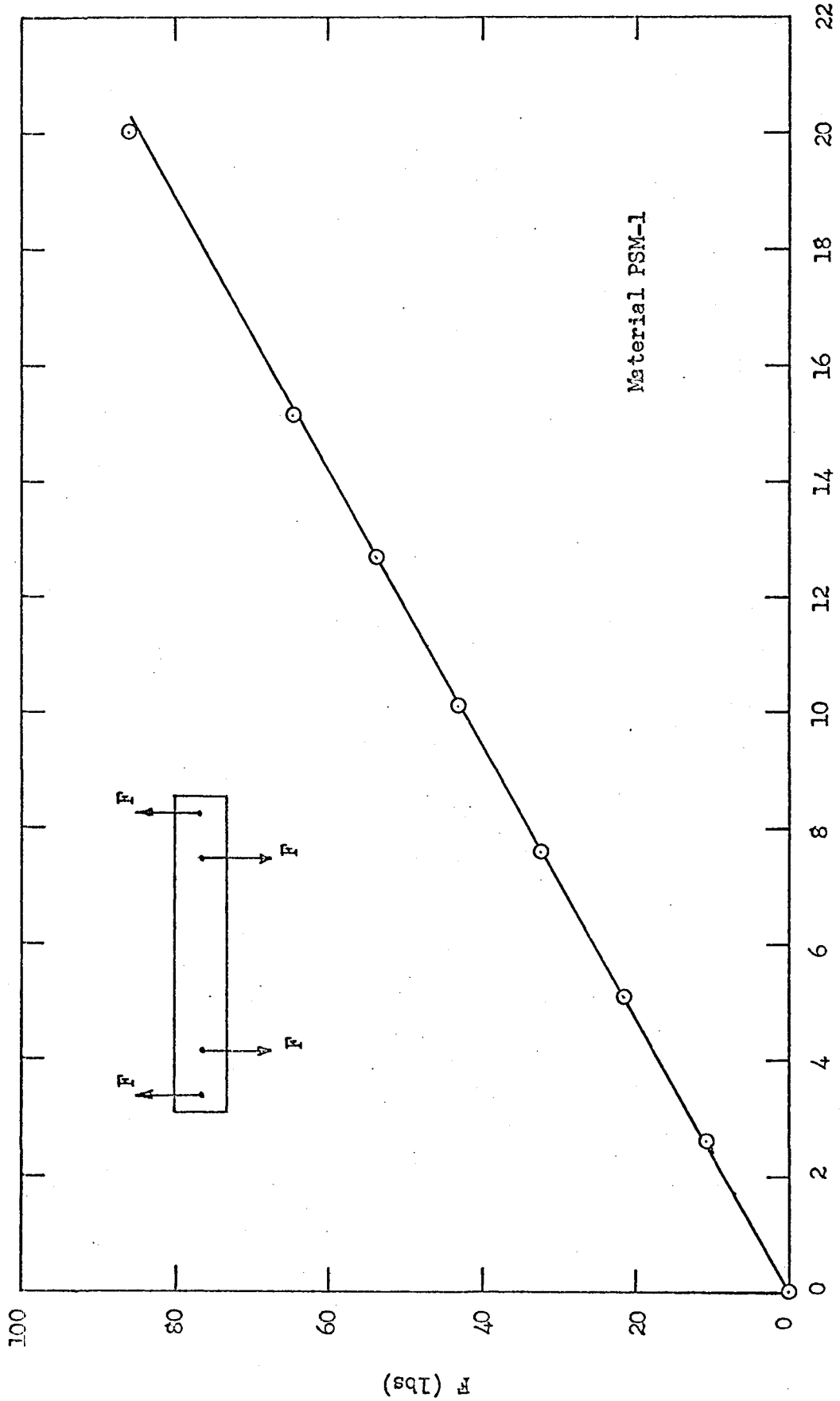

Fig. 17 Load against Fringe Order for a Beam in Pure Bending

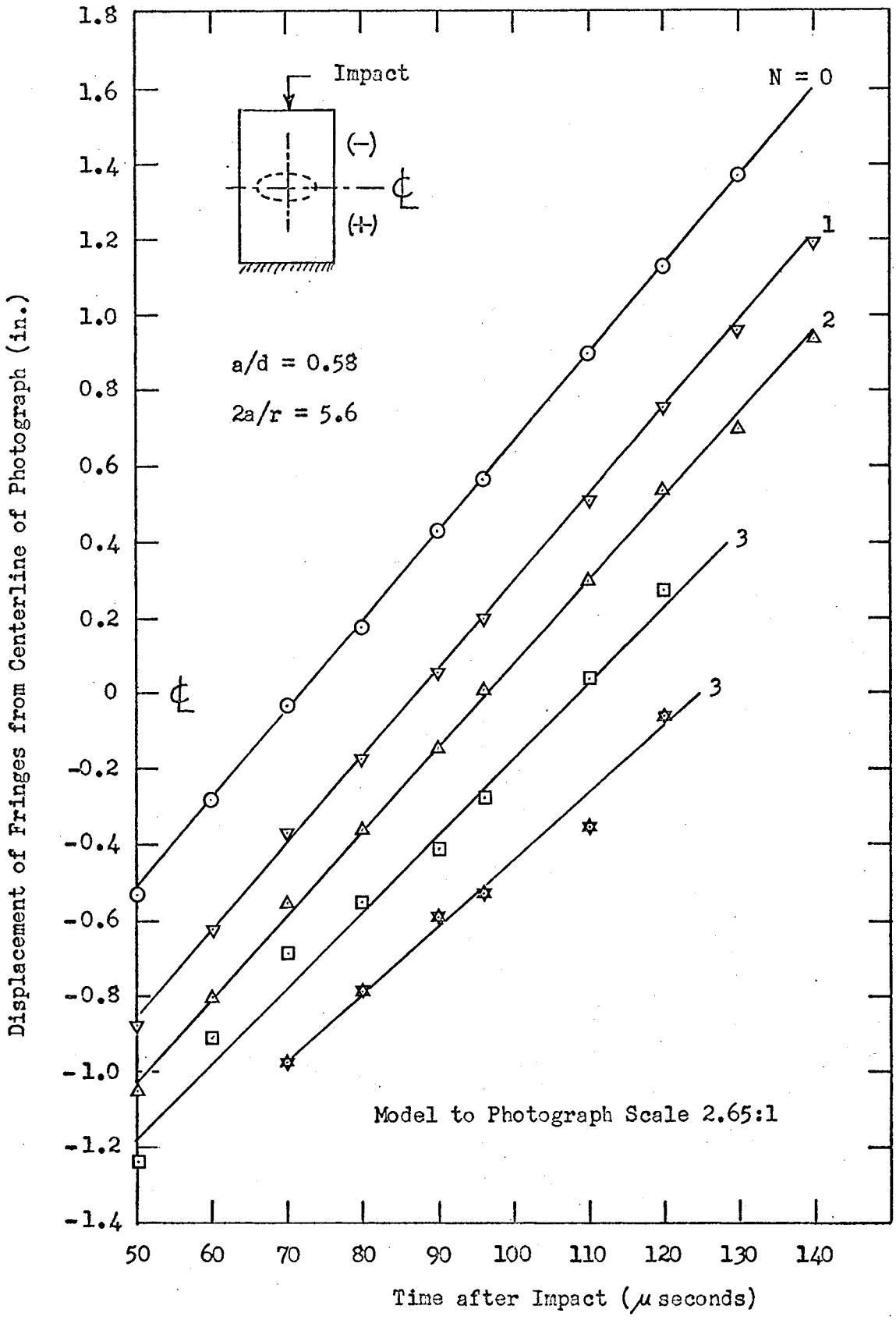

Fig. 18 Fringe Order Displacement on Photographs against Time after Impact

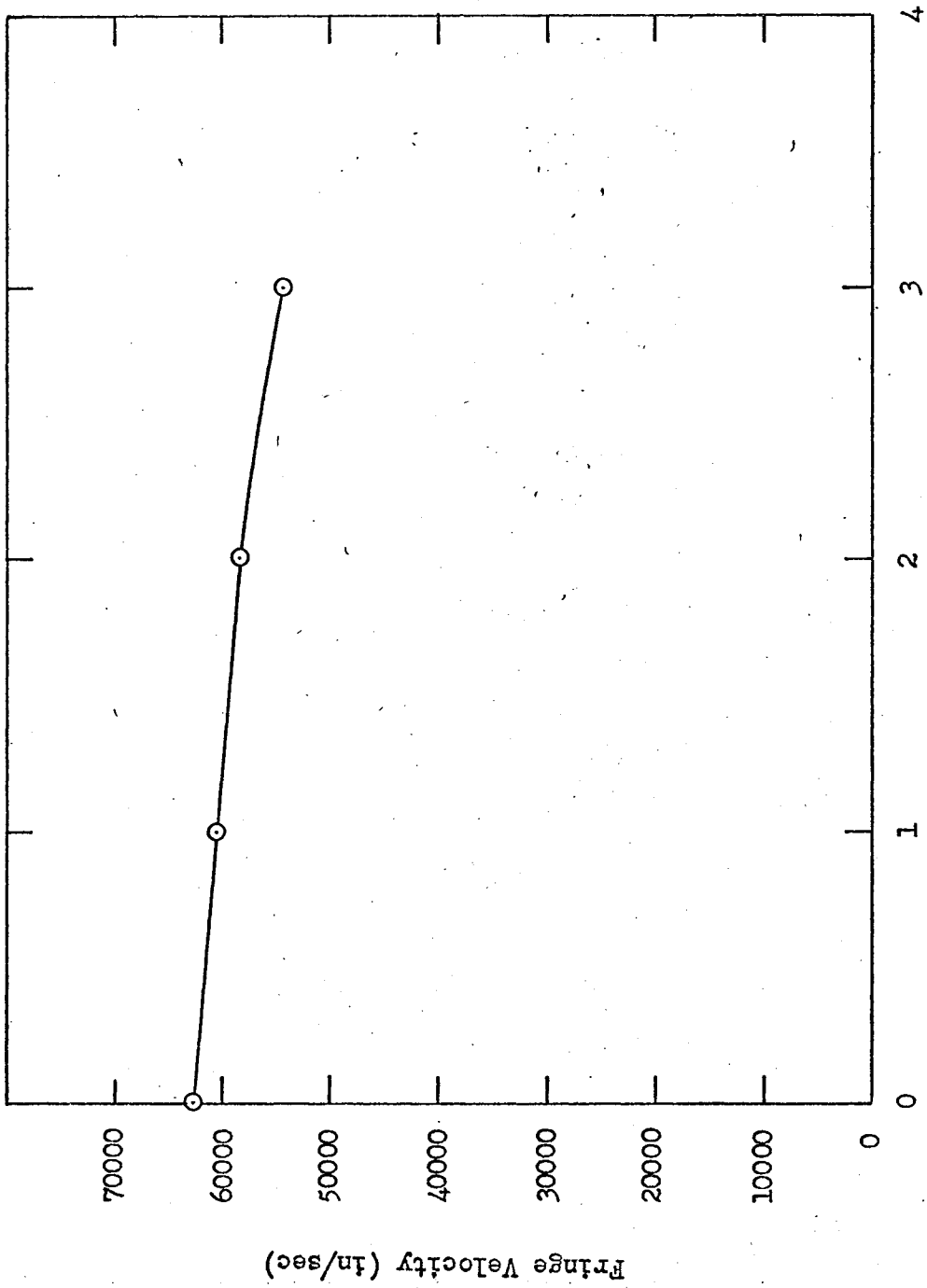

Fig. 19 Fringe Velocity against Fringe Order

APPENDIX B

THE MODULATED RUBY LASER LIGHT SOURCE

The laser output contains some very desirable characteristics which are quite compatible with the requirements of dynamic photoelasticity (24). These characteristics are shown in a tabulated form in the following table.

OUTPUT CHARACTERISTIC	REMARKS
Monochromatic	6943Å with a band width of 0.1Å
Parallel Output	Less than one degree divergence
Polarized	100 percent
Output Intensity ($watts/cm^2$)	For this system the output was 2 joules or 3500 $watts/cm^2$ based on random mode of operation. For Q-spoiled mode, the intensity increases by 2 orders of magnitude.
Spatial Coherence	Not of importance in this experiment but necessary in the field of holography.
With an input of 1000 joules (maximum for this system), the efficiency is 0.2% in the random lasing mode and an order of magnitude less in the Q-spoiled mode. The efficiency also depends on the mirrors bounding the lasing cavity.	

The intensity (3500 watts/cm^2) is based on the cross sectional area of the ruby (dia. = 3/8") and is calculated for 800 microseconds random lasing. This time can vary depending upon the condition of the laser.

B.1 . The Laser Head and Its associated Elements

Figure 20 shows a schematic arrangement of the laser head elements for the laser used in this experiment. The ruby and flash tube are placed in a highly reflective elliptical cavity with the ruby at one focus and the flash tube at the other focus. This is to ensure that the ruby receives as much of the flash tube light as possible. The flash tube receives 1000 joules from the laser head power supply (LPS8A) and supplies this energy to the ruby in approximately 2 milliseconds.

It has been found that in order to have sufficient amplification for lasing action, it is necessary to have a long lasing medium. Since this is not practical, a system of two reflecting mirrors producing a feedback system is used with the ruby rod between them. One mirror (48% reflective) is on one end of the ruby rod and the other mirror (99% reflective) is displaced so that a pockels cell and prism can be placed within the lasing cavity. The partially reflective mirror allows the output of the laser to escape after sufficient amplification has occurred. If optimum performance is expected, these mirrors must be lined up parallel to each other.

B.1.1 Operation in the Random Lasing Mode: If the pockels cell and prism are removed from the lasing cavity, the output appears as a number of randomly spaced spikes. This random lasing will continue for some 800 microseconds if the laser is in optimum operating condition. Using a photo multiplier output recorder (Appendix C) and an oscilloscope, the

random lasing shown in fig. 21 was obtained. Each spike in the photograph indicates lasing has occurred and the curvature of the sweep represents the flash tube envelope.

B.2 Operation in the Q-spoiled Mode.

To operate the laser in the Q-spoiled mode, a pockels cell and a prism are introduced into the lasing medium as shown in fig. 20. The pockels cell is an electrically sensitive birefringent crystal that produces half wave retardation for the 6943Å red ruby output at 12KV potential and the prism is nothing more than a good polarizer. For operation, the polarization axis of the prism and y axis of the pockels cell must be oriented to a position parallel to the polarization axis of the ruby and to minimize losses, the faces of the prism and cell must be parallel to the mirrors.

When the polarized ruby light enters the energized pockels cell, it is split into two equal orthogonal components which are in phase but at 45 degrees to the initial ruby axis of polarization. When the components emerge from the cell, the relative phase difference between them is 180 degrees. Thus, the vector sum of these components is equal in magnitude to the incident polarized ruby light but at 90 degrees to the axis of ruby polarization. This light is now absorbed by the prism since the axis of polarization of this prism is parallel to the axis of polarization of the ruby. Thus, no amplification occurs and lasing is held off. If, however, the cell voltage is removed, the light from the ruby will pass through the prism and to the mirror. Amplification due to oscillations in the lasing cavity can now occur and a very short (0.1 microseconds) intense, Q-spoiled light pulse emerges from the laser.

The pockels cell voltage must then be quickly re-established to stop random lasing from following a Q-spoiled pulse. The two photographs in fig. 21 show the difference between random lasing and Q-spoiling. The Q-spoiled pulse is so very short that the oscilloscope (Tektronix type 564) is unable to record it faithfully although its position is identified by a break in the sweep.

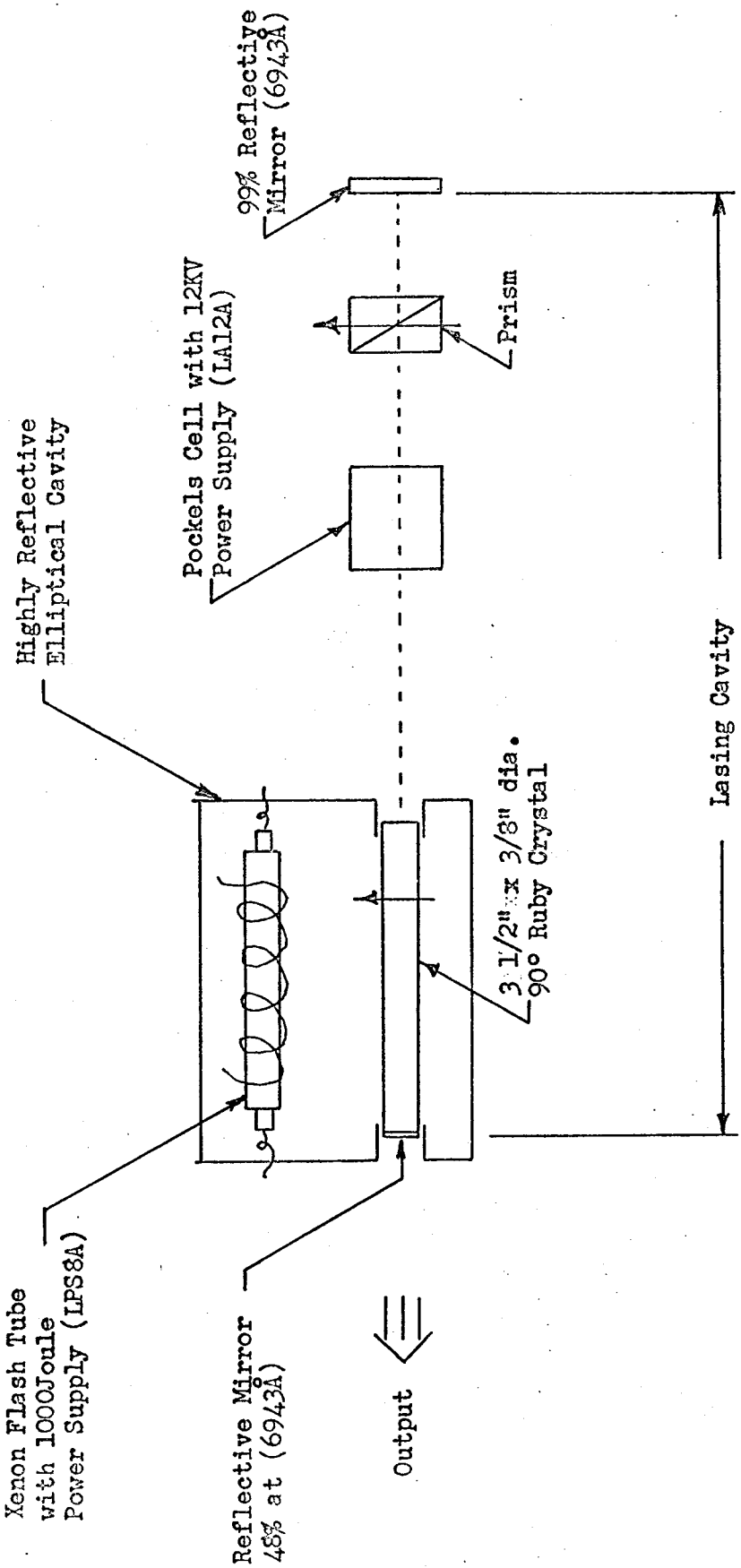

Fig. 20 Schematic Diagram of the Laser Head and its Elements

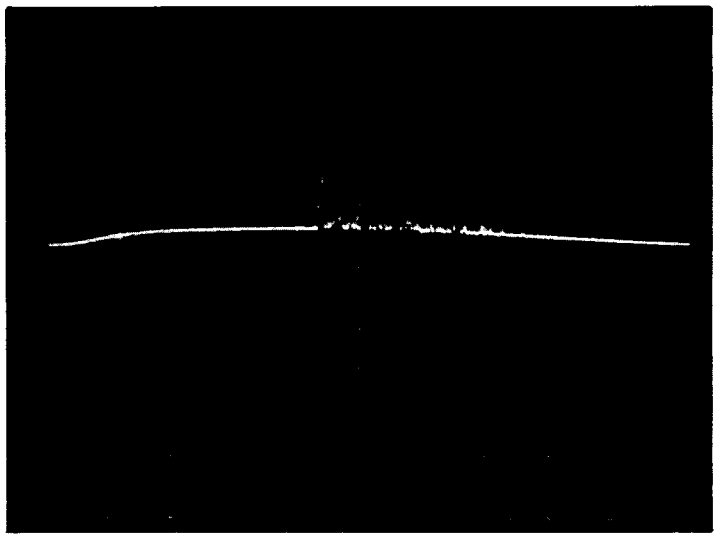

Random Lasing

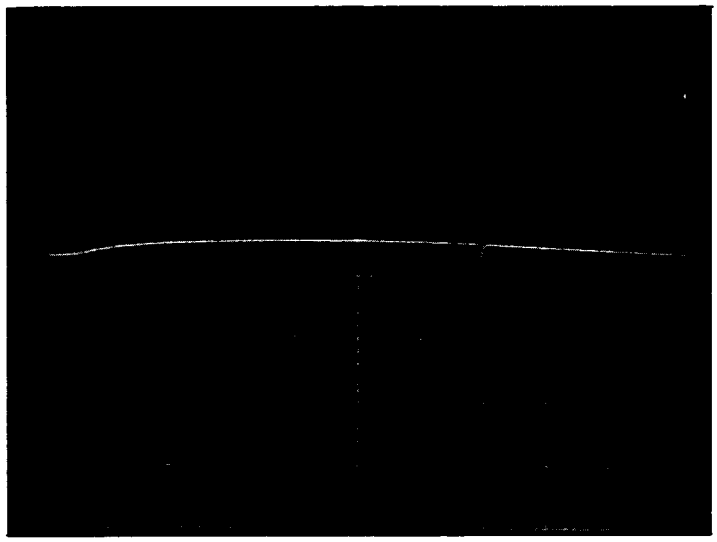

Q-Spoiled Pulse
vertical scale, 0.05v/cm
horizontal scale, 200μsec/cm

Fig.21 Random Lasing and Q-Spoiling Photographs

APPENDIX C

THE AUXILIARY EQUIPMENT AND ITS OPERATION

C.1 Loading Mechanism.

In this experiment, the dynamic load was produced by a 22 caliber projectile from an air pistol. The pistol was modified to accept nitrogen from a welders' tank which was released to the gun by a pressure reducing regulator set to a constant pressure of 500 psig. Two separate triggering systems consisting of a photocell and a mechanical trigger were incorporated as part of the loading mechanism such that the laser output could be synchronized with the load cycle. A cycle begins as the pellet first activates a photocell and the resulting electrical pulse after being amplified and delayed, triggers the laser head power supply to release energy to the laser.

The pellet activated mechanical trigger which consisted of a steel model cap and a steel plunger was designed to simultaneously load the model and close an electrical contact. The metal cap, as shown in fig. 1, was placed in contact with the end of the model. The 0.73 oz. plunger separated from the cap by 3/32 inches was held in place by strong return springs under initial tension and requiring a static force of 5.5 lb. to bring the plunger in contact with the model cap. Figure 22(a) shows that the electrical output pulse from the mechanical trigger was approximately 30 microseconds in duration. Thus, the load duration was no more than 30 microseconds and could have been as little as 15 microseconds.

The time after impact was measured from the instant of plunger contact. This resulting trigger pulse after being delayed was then used to trigger a Q-spoiled pulse from the laser. Although this would appear to be difficult to control accurately, it is estimated that the experiment could be repeated with an accuracy of 2 microseconds at a constant delay setting for the interval of time (50 to 140 microseconds) studied here representing an average error (in time) of only 2%. This estimate is based on the similarity between photographs obtained for a constant time after impact. The average shell velocity over a distance of 12 3/16 inches for eleven separate tests was 360 ft/sec.

The following sequence of events in conjunction with fig. 23 describes what took place to obtain each photograph for a particular delay time (t) after impact.

A. The amplified photocell pulse triggers the delay in the pulse generator.

B. The laser power supply is triggered and immediately energy is released to the flash tube.

C. This is the time interval for the pellet to travel from some location beyond the photocell to the mechanical trigger at the top of the model.

D. At this point, the model is loaded and simultaneously an electrical pulse enters the pockels cell delay circuit to be delayed a time (t).

E. At the end of time (t), the pockels cell bias voltage is removed and immediately thereafter a Q-spoiled laser spike occurs.

F. Random lasing would occur for approximately 800 microseconds if the pockels cell is not used.

G. This interval represents the approximate time that energy is supplied to the flash tube.

C.2 Equipment Circuit Diagrams.

The following subsections describe the equipment which was built by the Electrical Division of The Central Research Shop at the University of Windsor.

C.2.1 Photocell and Amplifier Circuit: Figure 24 shows the photocell circiut. The rise time of the output pulse was 50 microseconds and the peak voltage was 0.05 volts. This pulse was delivered to the amplifier where it was amplified to 3 volts peak. Figure 25 shows the amplifier circuit and the photograph in this figure shows the output pulse from the amplifier.

C.2.2 Mechanical Trigger and Multiple Pulse Hold-Off Circuit: Figure 26 shows the mechanical trigger and multiple pulse hold-off circuit. The top trace of photograph (b) shown in fig. 22 is the mechanical trigger output and the bottom trace is the output from the multiple pulse hold-off circuit. The mechanical trigger shows two step pulses about 600 microseconds apart. The second step pulse is due to contact bounce and produces electrical contact but no load on the model. Since this second pulse could trigger the laser a second time and further expose the birefringence photographs, the multiple pulse hold-off circuit was designed to accept only the first and most important step pulse.

C.2.3 Laser Output Recording System: The laser output recorder shown in fig. 27 is capable of a rise time of 10 nanoseconds. This is necessary since the laser spikes have a rise time and duration in the order of nanoseconds. The output recorder was placed behind the 99% reflective mirror where it received flash tube light and approximately 1% of the

laser light. The associated power supply is shown in fig. 28. The design of the recording system was obtained from reference (24).

C.3 The Commercial Equipment Used.

The following list of equipment was used.

1. Crossman Mark I (0.22 caliber) single shot co_2 pistol.
2. Milbro "Caledonian" waisted pellets (0.22 caliber) manufactured in Great Britain.
3. Hewlett Packard Pulse Generator (model 222A) and two D.C. power supplies (model 721A).
4. Raytheon Laser
   (a) Laser head (LH6) delivering 2 joules output with a $3\frac{1}{2}$ in. long by 3/8 in. diameter ruby.
   (b) Power supply (LPS8A) delivering 1000 joules.
   (c) Pockels cell Q-switch containing a potassium dihydrogen phosphate (KDP) birefringent crystal.
   (d) Pockels cell power supply (LA12A) capable of 0-15 KVDC and containing a delay circuit with a range of 5 microseconds to 3 milliseconds.
5. Graphlex camera with extension bellows and used with $3\frac{1}{4}$ in. X $4\frac{1}{4}$ in. infrared Polaroid film type 413.
6. Tektronix (564) storage oscilloscope with type 3A1 dual trace amplifier and type 3B3 time base plug-in units.

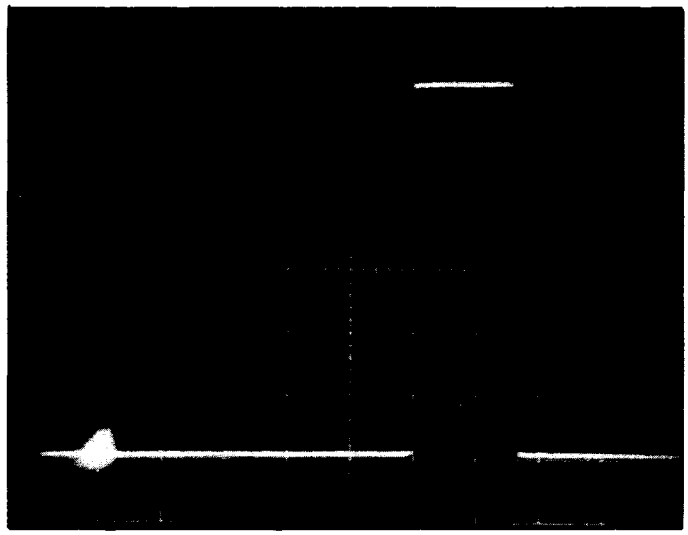

(a)

Mechanical Trigger Output--horizontal scale 20μsec/cm, vertical scale 1v/cm

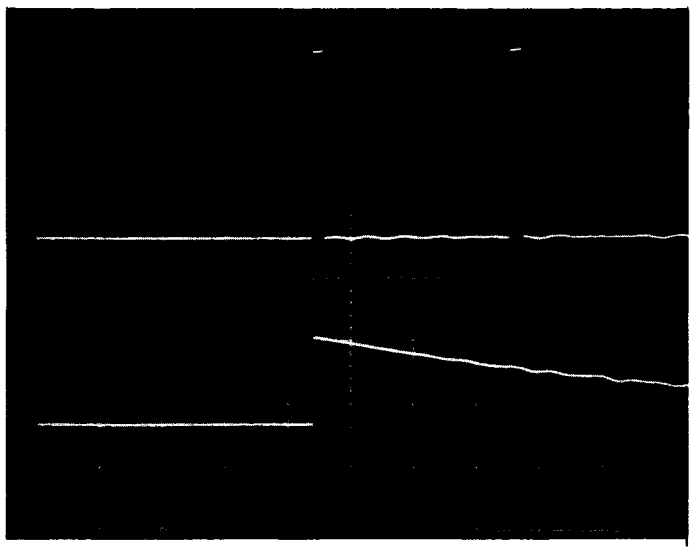

(b)

Upper Trace--Mechanical Trigger Output(2v/cm)
Lower Trace--Multiple Pulse Hold-Off Output(10v/cm)
horizontal scale 200μsec/cm

Fig. 22 Output Pulse of Mechanical Trigger and Multiple Pulse Hold-Off Circuits

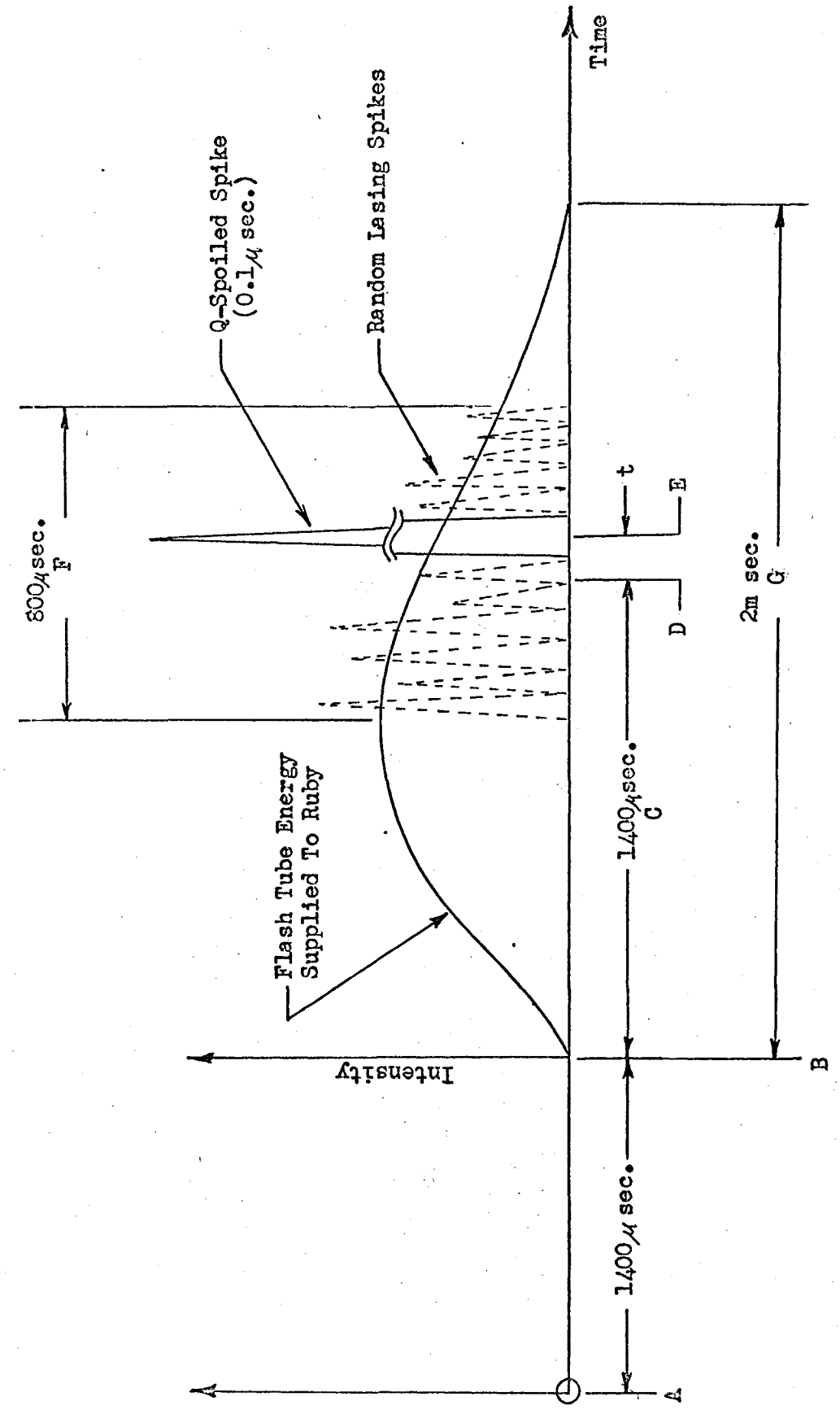

Fig. 23 Schematic Diagram of the Events to obtain Each Photograph

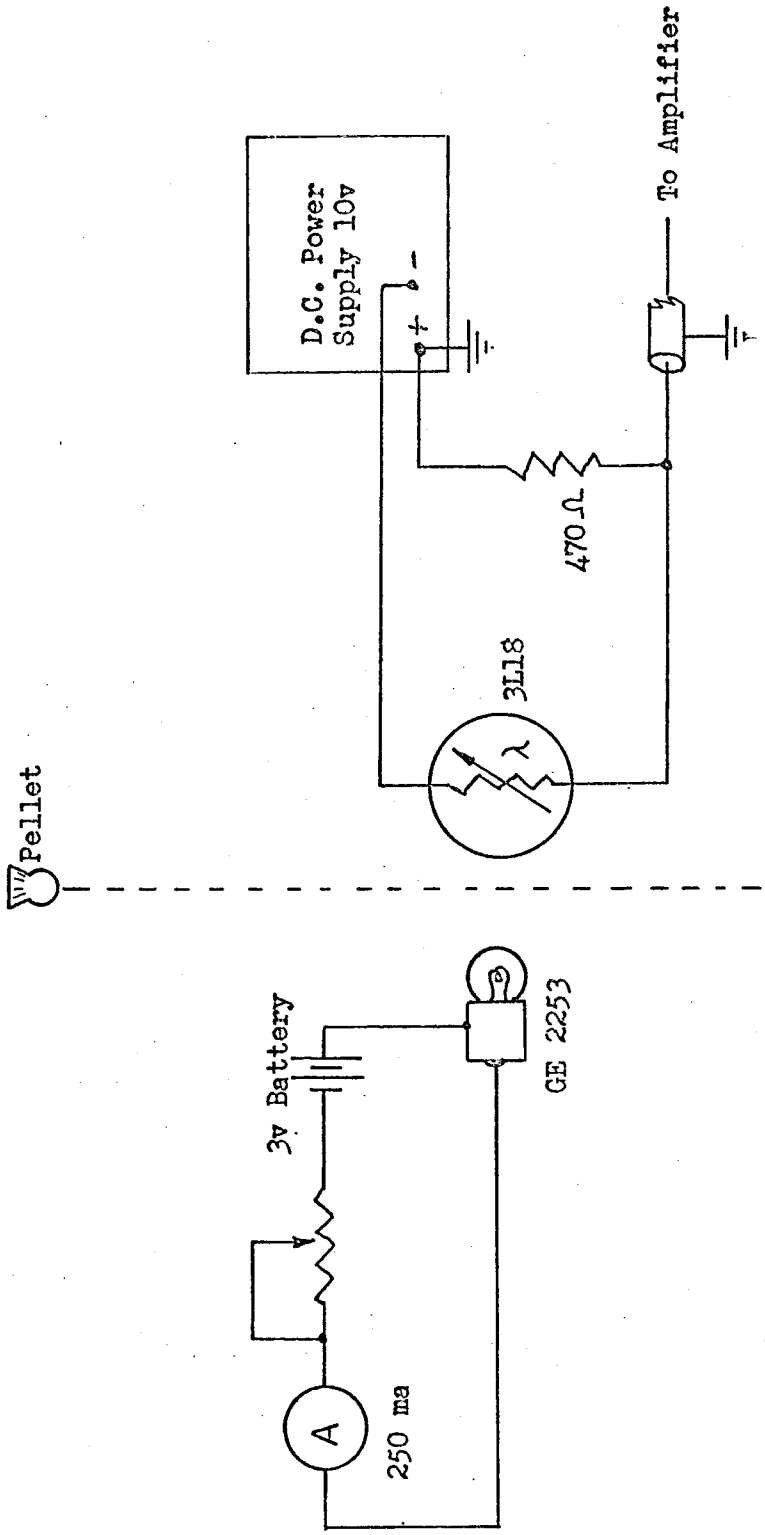

Fig. 24 Photocell Circuit Diagram

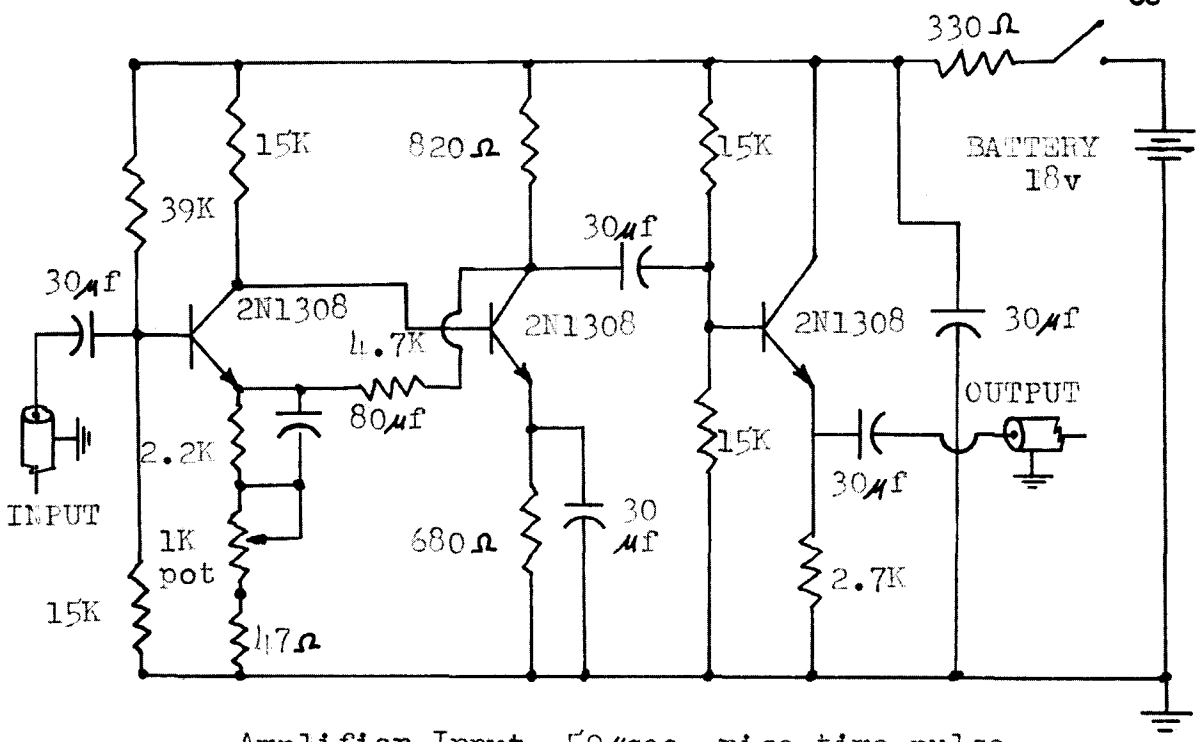

Amplifier Input--50μsec. rise time pulse
with peak voltage of 0.05volts

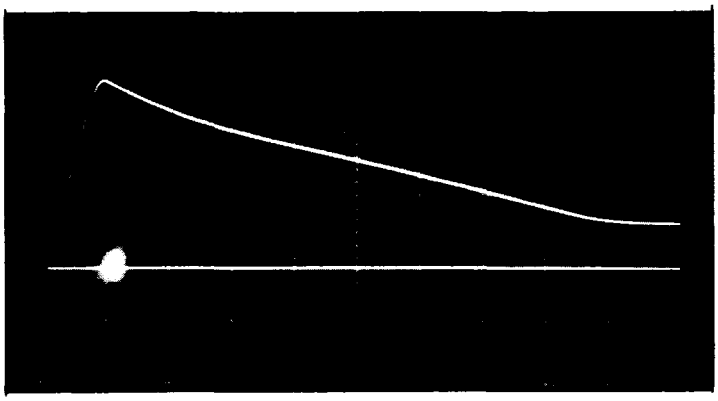

Amplifier Output Trace
vertical scale-1v/cm
horizontal scale-50μsec/cm

Fig.25 Photocell Amplifier Circuit Diagram

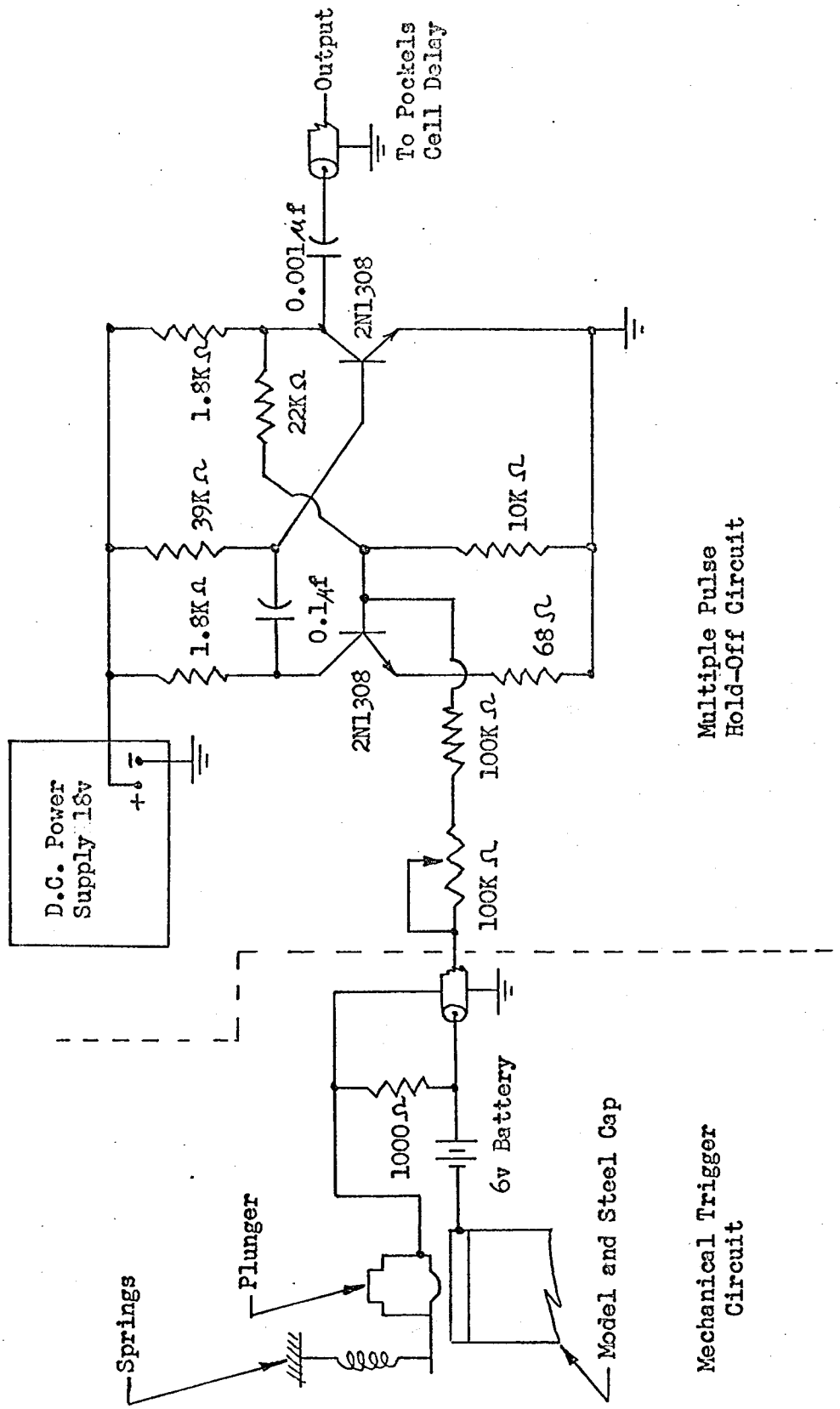

Fig. 26 Mechanical Trigger and Multiple Pulse Hold-Off Circuit

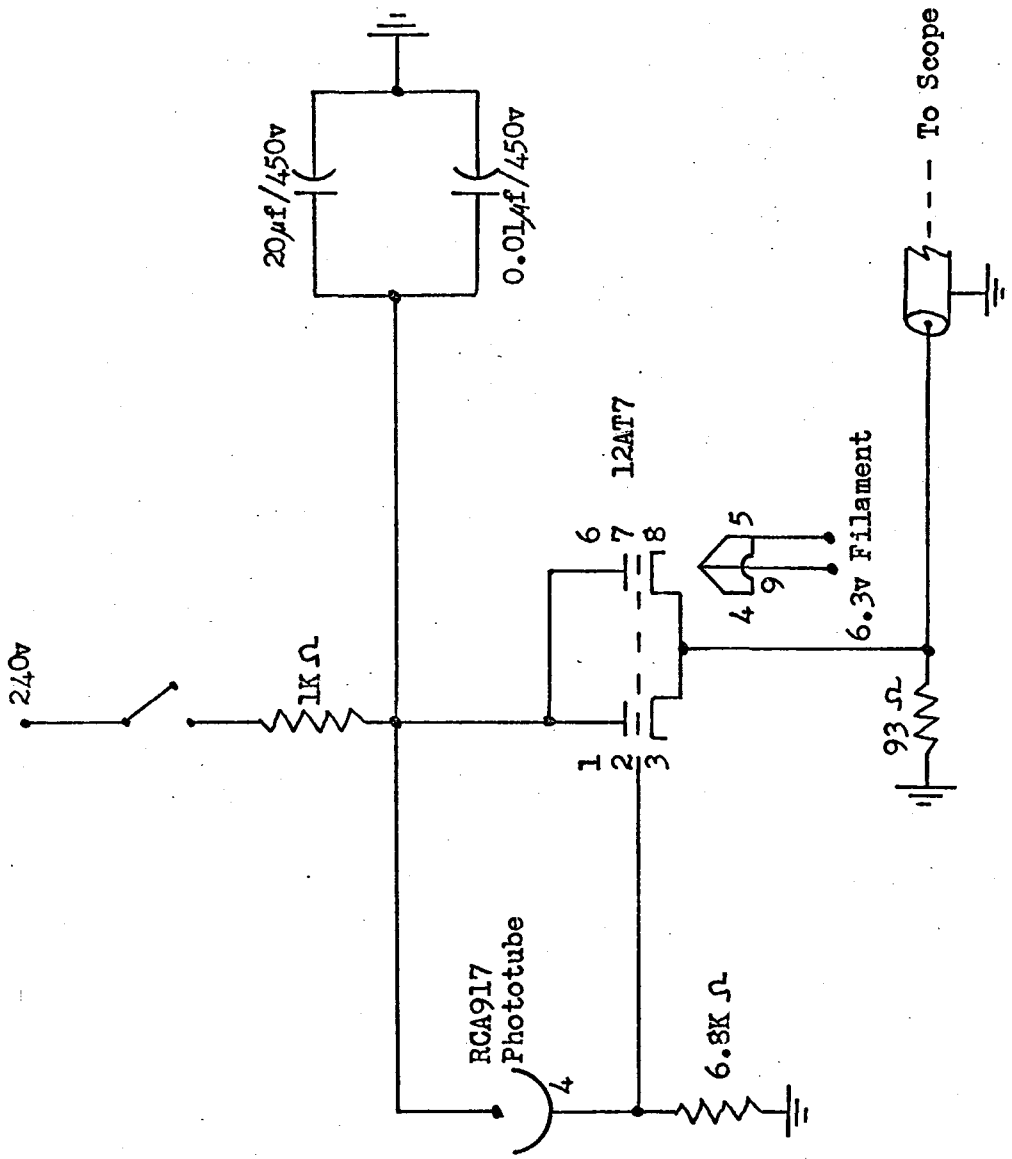

Fig. 27 Laser Output Recorder Circuit

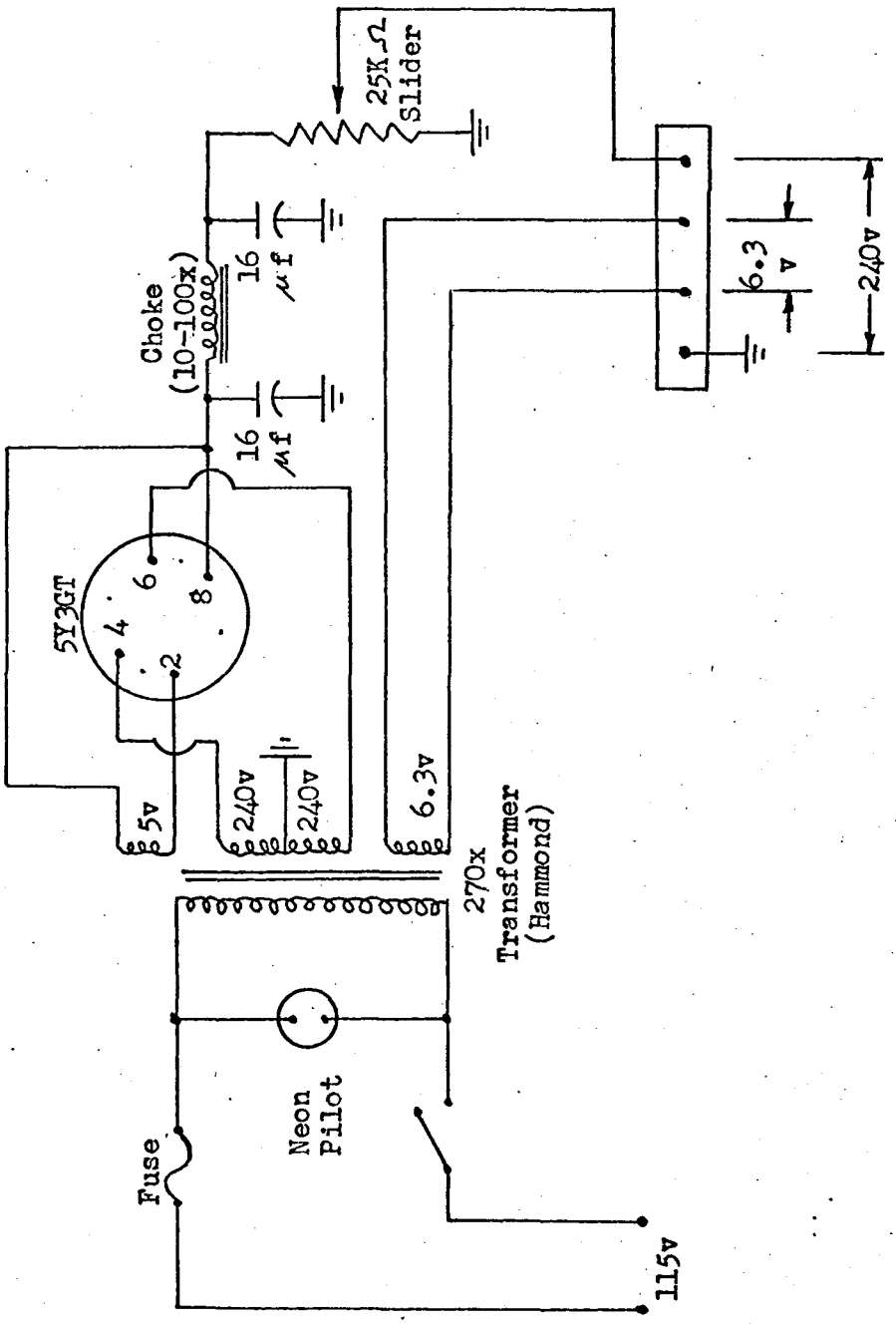

Fig. 28 Laser Output Recorder Power Supply Circuit

VITA

1938 Born in Goderich, Ontario, Canada.

1961 Graduated from the Western Ontario Institute of Technology Windsor, Ontario, as a Mechanical Technologist.

1961-63 Mechanical Technologist at the National Research Council Ottawa, Ontario.

1966 Received the degree of Bachelor of Applied Science in Mechanical Engineering from the University of Windsor, Windsor, Ontario.

1968 Presently a candidate for the degree of Master of Applied Science in Mechanical Engineering at the University of Windsor.